Discontinuous Galerkin modeling of the Columbia River's coupled estuary-plume dynamics

Vallaeys, Valentin; Kärnä, Tuomas; Delandmeter, Philippe; Lambrechts, Jonathan; Baptista, António M.; Deleersnijder, Eric; Hanert, Emmanuel

Important note
To cite this publication, please use the final published version (if applicable).
Please check the document version above.

Discontinuous Galerkin modeling of the Columbia River's coupled estuary-plume dynamics

Valentin Vallaeys*[1], Tuomas Kärnä[2], Philippe Delandmeter[1,3], Jonathan Lambrechts[1], António M. Baptista[2], Eric Deleersnijder[4,5], and Emmanuel Hanert[6]

[1]Université catholique de Louvain, Institute of Mechanics, Materials and Civil Engineering (iMMC), 4 Avenue G. Lemaître, B-1348 Louvain-la-Neuve, Belgium

[2]NSF Science and Technology Center for Coastal Margin Observation & Prediction, Oregon Health & Science University, Portland, OR, USA

[3]Utrecht University, Institute for Marine and Atmospheric research, Utrecht, The Netherlands

[4]Université catholique de Louvain, Institute of Mechanics, Materials and Civil Engineering (iMMC) & Earth and Life Institute (ELI), 4 Avenue G. Lemaître, B-1348 Louvain-la-Neuve, Belgium

[5]Delft University of Technology, Delft Institute of Applied Mathematics (DIAM) Mekelweg 4, 2628CD Delft, The Netherlands

[6]Université catholique de Louvain, Earth and Life Institute (ELI), Croix du Sud 2 box L7.05.16, B-1348 Louvain-la-Neuve, Belgium

February 22, 2018

*valentin.vallaeys@uclouvain.be

Abstract

The Columbia River (CR) estuary is characterized by high river discharge and strong tides that generate high velocity flows and sharp density gradients. Its dynamics strongly affects the coastal ocean circulation. Tidal straining in turn modulates the stratification in the estuary. Simulating the hydrodynamics of the CR estuary and plume therefore requires a multi-scale model as both shelf and estuarine circulations are coupled. Such a model has to keep numerical dissipation as low as possible in order to correctly represent the plume propagation and the salinity intrusion in the estuary. Here, we show that the 3D baroclinic discontinuous Galerkin finite element model SLIM 3D is able to reproduce the main features of the CR estuary-to-ocean continuum. We introduce new vertical discretization and mode splitting that allow us to model a region characterized by complex bathymetry and sharp density and velocity gradients. Our model takes into account the major forcings, i.e. tides, surface wind stress and river discharge, on a a single multi-scale grid. The simulation period covers the end of spring-early summer of 2006, a period of high river flow and strong changes in the wind regime. SLIM 3D is validated with in-situ data on the shelf and at multiple locations in the estuary and compared with an operational implementation of SELFE. The model skill in the estuary and on the shelf indicate that SLIM 3D is able to reproduce the key processes driving the river plume dynamics, such as the occurrence of bidirectional plumes or reversals of the inner shelf coastal currents.

Keywords

- Unstructured mesh

- Multi-scale model

- River-to-ocean continuum

- Plume dynamics

- Columbia River estuary

1 Introduction

The Columbia River (CR) is the main river of the western coast of North America. Its discharge is on average around 8×10^3 m^3/s and regularly exceeds 10^4 m^3/s. The CR estuary alternates between a moderately and a strongly stratified system. Based on the estuary classification scheme of Geyer and MacCready (2014), Kärnä and Baptista (2016a) identified four dominant regimes corresponding to a combination of high/low flow and spring/neap tidal conditions. The CR is a mesotidal river, with a maximum tidal range varying from 1.7 m to 3.8 m. These characteristics induce large surface velocities and density fronts at the mouth during ebbs.

Water outflowing from the CR mouth spreads into the Pacific ocean, forming a river plume. Horner-Devine et al. (2009) split this complex body into four main water masses: the source water and the tidal, re-circulating and far-field plumes. The source water is the estuarine low-salinity water detaching from the ground to create the plume. The tidal plume is the pulse of brackish waters outflowing from the mouth of the estuary every ebb tide with a timescale of 6-12 hours. The re-circulating plume, also called the bulge, is the near-field part of the plume waters on the shelf, mostly driven by the Coriolis force and the river momentum flux. These waters stay on the shelf for a period of 0.5 to 4 days. The far-field plume is the discharged waters beyond the re-circulating plume generating the coastal currents, with a retention timescale of roughly 1 week. The development of the three coastal plume regions can be observed under low wind conditions.

Strong winds can significantly modify the re-circulating and far-field plumes dynamics. The Ekman theory states that wind-driven coastal upwelling (resp. downwelling) is generated in the northern hemisphere when the coast lays left (resp. right) of the wind blowing direction. As the surface water moves offshore it is replaced by water that wells up from below, a process known as coastal upwelling. This creates major changes in the development of the plume as reversals in wind lead to rapid changes in the plume orientation (Fiedler and Laurs, 1990; Garcia Berdeal et al., 2002; Hickey et al., 2005). Downwelling-favorable winds tend to enhance and narrow the northern coastal current, erasing the re-circulating plume. Sufficiently strong southward upwelling-favorable winds erode the coastal current and drive the extended plume offshore.

The plume has a significant influence on the biochemical processes occurring on the shelf. The river plume provides a habitat for Pacific salmon, affects plankton growth, advects primary production offshore and is partly responsible for the higher primary production off the Washington coast compared to the Oregon coast where the wind regime suggests stronger upwelling south of the CR mouth (Hickey and Banas, 2003; Burla et al., 2010; Davis et al., 2014; Giddings et al., 2014; Phillips et al., 2017). The presence of the CR plume also increases the cross-shelf transport of nutrient-rich upwelled waters (Hickey et al., 2009). Accurate modeling of the CR coastal ocean dynamics is fundamental to fully understand its implications on the California Current system and its ecosystem.

The challenge of modeling the CR plume dynamics arises from the strong coupling with the estuarine dynamics, the presence of sharp gradients of bathymetry, velocity and density, and the dependence to external forcings such as tides, winds or river discharges. Earlier numerical

modeling studies of the CR estuary and adjacent coastal sea have been carried out by means of three dimensional circulation models. After successfully simulating the whole estuary-to-plume dynamics of the CR with ELCIRC (Zhang and Baptista, 2004; Zhang et al., 2004; Baptista et al., 2005), Zhang and Baptista (2008) produced better results in the CR estuary by using SELFE, an unstructured mesh model that allows more geometrical flexibility than ELCIRC. This model reproduced the circulation of the estuary and coastal region, enabling a good representation of the plume and coastal up/down-welling (Burla et al., 2010). SELFE skill has been mostly assessed and quantified within the estuary (Kärnä et al., 2015; Kärnä and Baptista, 2016a). There have been fewer applications of SELFE to model the plume variability (Burla et al., 2010). In MacCready et al. (2009), another successful representation of the global hydrodynamics in this region is described using ROMS (Haidvogel et al., 2000). Further skill assessment for this model was carried both on the shelf and in the estuary (Liu et al., 2009b). One major issue of SELFE is the inability to represent the complete gravitational circulation, causing the model to underestimate salinity intrusion under neap tides conditions (Kärnä et al., 2015). The numerical dissipation prevents to capture the sharp stratification. Lopez and Baptista (2017) highlight the difficulty of the SELFE sediment module to reproduce the sediment dynamics as the stratification is one of the key process at stake. Furthermore, this dissipation is detrimental on the shelf where the sharp fronts of the plume are smoothed out. This prevents capturing small scale variability of the plume despite high mesh resolution. Major issues with ROMS are the use of structured grids, the approximation of the upper river by a long straight channel and the need to strongly smooth the bathymetry, leading to a spurious deepening of the estuarine channels (MacCready et al., 2009). A better model would tackle major issues of both models: low numerical dissipation and unstructured multi-scale mesh.

Here we use the three-dimensional version of the Second-generation Louvain-la-Neuve Ice-ocean Model (SLIM 3D, www.climate.be/slim) to simulate the Columbia river-to-sea continuum. SLIM is an unstructured mesh discontinuous Galerkin finite element model. The depth-averaged 2D version of SLIM has been applied to a variety of coastal areas including the Great Barrier Reef (Lambrechts et al., 2008; Thomas et al., 2014), the Scheldt estuary (de Brye et al., 2010), the Congo River (Le Bars et al., 2016), the Mahakam River (de Brye et al., 2011; Pham Van et al., 2016), and even a lake on Titan (Vincent et al., 2016). The main drawback of discontinuous Galerkin (DG) methods is the larger number of degrees of freedom per element, which results in a higher computational cost than continuous Galerkin (CG) methods. The data structure of DG methods however makes them better suited to parallel computing architectures. Here we use the 3D baroclinic version of SLIM. It solves the hydrostatic equations under Boussinesq approximation (White et al., 2008; Blaise et al., 2010; Comblen et al., 2010; Kärnä et al., 2013). In order to include a realistic large scale ocean circulation in the model, we have improved SLIM 3D by adding z layers, boundary conditions with stratified density and velocity fields and an improved mode splitting algorithm.

The goal of this study is to model the CR plume and estuary by means of SLIM 3D, provide a qualitative and quantitative validation against sets of observations in the estuary and on the shelf, and compare SLIM 3D to an operational implementation of SELFE. We first evaluate the ability of SLIM 3D to simulate all major hydrodynamical regimes of the CR estuary and

plume. We then study the evolution of the CR plume under realistic wind conditions. Data and methods are detailed in Section 2. The model is then validated against a large set of observations and compared to SELFE (Section 3), which helps us gain insight on the CR plume variability (Section 4). Discussion and perspectives for future work are in Section 5.

2   Material and methods

SLIM 3D is a hydrodynamical model solving the 3D hydrostatic equations under Boussinesq approximation by means of a discontinuous Galerkin discretization. It has been validated against a number of idealized baroclinic test cases (Kärnä et al., 2013) as well as for fine sediments dynamics in a very shallow semi-open basin in the Great Barrier Reef (Delandmeter et al., 2015). Both cases consisted in a rather shallow area with a smooth bathymetry. The CR study is the first attempt to apply SLIM 3D to a complex river-estuary-plume system that includes a shelf break.

Compared to the previous version of SLIM 3D (Delandmeter et al., 2015), the main improvements are:

- Enhanced flexibility in the generation of the vertical grid. As explained in Section 2.3, SLIM 3D now enables any user-defined vertical grids: terrain-following, staircase-like z, or any combination of it.

- Depth-dependent boundary conditions at the open boundaries. Before the present study, only depth-integrated tidal transport or river discharges could be imposed.

- New mode-splitting formulation. Based on the work of Higdon and de Szoeke (1997), the 2D external mode equations have been simplified by keeping only the Coriolis and the external pressure gradient terms. All the other terms are merged together in a vertically-averaged force term.

The current formulation of SLIM 3D and all the implementation details are presented below.

2.1   Numerical model

SLIM 3D solves the 3D hydrostatic equations under Boussinesq approximation:

$$\frac{\partial \boldsymbol{u}}{\partial t} + \boldsymbol{\nabla}_h \cdot (\boldsymbol{u}\boldsymbol{u}) + \frac{\partial (w\boldsymbol{u})}{\partial z} = \boldsymbol{\nabla}_h \cdot \left(\nu_h \left(\boldsymbol{\nabla}_h \boldsymbol{u} + (\boldsymbol{\nabla}_h \boldsymbol{u})^T \right) \right) + \frac{\partial}{\partial z} \left(\nu \frac{\partial \boldsymbol{u}}{\partial z} \right)$$
$$- f\boldsymbol{e}_z \wedge \boldsymbol{u} - \frac{1}{\rho_0} \boldsymbol{\nabla}_h p, \tag{1}$$

$$\boldsymbol{\nabla}_h \cdot \boldsymbol{u} + \frac{\partial w}{\partial z} = 0, \tag{2}$$

$$\frac{1}{\rho_0} \boldsymbol{\nabla}_h p = g\boldsymbol{\nabla}_h \eta + \frac{g}{\rho_0} \boldsymbol{\nabla}_h \int_z^\eta \left(\hat{\rho}(S,T) - \rho_0 \right) d\zeta, \tag{3}$$

$$\frac{\partial S}{\partial t} + \boldsymbol{\nabla}_h \cdot (\boldsymbol{u}S) + \frac{\partial (wS)}{\partial z} = \boldsymbol{\nabla}_h \cdot (\kappa_h \boldsymbol{\nabla}_h S) + \frac{\partial}{\partial z} \left(\kappa \frac{\partial S}{\partial z} \right), \tag{4}$$

$$\frac{\partial T}{\partial t} + \boldsymbol{\nabla}_h \cdot (\boldsymbol{u}T) + \frac{\partial (wT)}{\partial z} = \boldsymbol{\nabla}_h \cdot (\kappa_h \boldsymbol{\nabla}_h T) + \frac{\partial}{\partial z} \left(\kappa \frac{\partial T}{\partial z} \right), \tag{5}$$

where the variables are the horizontal velocity, $\boldsymbol{u}$, the vertical velocity, w, the pressure, p, the surface elevation, η, the salinity, S, and the temperature, T. The symbol $\boldsymbol{\nabla}_h$ stands for the horizontal gradient operator. The equation for the pressure results from the hydrostatic hypothesis. The equation of state from Jackett et al. (2006) is used for the density $\hat{\rho}(S,T)$, while $\rho_0 = 1027$ kg/m^3 is the constant reference density. The material parameters are the Coriolis frequency f, the horizontal and vertical viscosities ν_h and ν and the horizontal and vertical diffusivities for κ_h and κ. Horizontal viscosity ν_h follows the Smagorinsky (1963) parametrization with $C_D = 0.02$. Vertical eddy viscosity ν and diffusivity κ are determined from the k-ϵ turbulence closure model of GOTM that is coupled to SLIM 3D (Kärnä et al., 2012) with Canuto A stability functions (Canuto et al., 2001). The bottom friction is computed with the law of the wall, assuming a logarithmic profile of velocity. The bottom roughness length, z_0, is set constant to 5×10^{-4} m.

In the previous version of SLIM 3D, fast propagating gravity waves were represented by the traditional two-dimensional depth-integrated shallow water equations. Until now, the splitting between 2D and 3D equations was not exact. For example, the Manning coefficient of the 2D bottom stress parametrization does not perfectly match the value computed with the law of the wall in 3D. This leads to a mismatch between the 2D and 3D modes. Constraining the conformity between modes smooths the velocity field, and the model tends to be too dissipative to correctly represent complex baroclinic flows. Following Higdon and de Szoeke (1997), we adapted the model formulation such that the mode splitting becomes exact. All the 3D forcing and coupling terms are now gathered together into a single term, denoted $\boldsymbol{G}$, yielding:

$$\frac{\partial \eta}{\partial t} + \boldsymbol{\nabla}_h \cdot (H\bar{\boldsymbol{u}}) = 0, \tag{6}$$

$$\frac{\partial \bar{\boldsymbol{u}}}{\partial t} + f\boldsymbol{e}_z \wedge \bar{\boldsymbol{u}} + g\left(1 + \frac{\rho_s'}{\rho_0}\right) \boldsymbol{\nabla}_h \eta = \boldsymbol{G}, \tag{7}$$

with the vertically averaged horizontal velocity $\bar{\boldsymbol{u}} = \frac{1}{H} \int_{-h}^{\eta} \boldsymbol{u} \, dz$, $\rho_s' = \hat{\rho}_s(S, T) - \rho_0$ the density deviation at the top surface and $H = h + \eta$ the total water column depth.

By substracting Eq. 7 from Eq. 1, we obtain an equation for $\boldsymbol{u}' = \boldsymbol{u} - \bar{\boldsymbol{u}}$:

$$\frac{\partial \boldsymbol{u}'}{\partial t} + \boldsymbol{\nabla}_h \cdot (\boldsymbol{u}\boldsymbol{u}) + \frac{\partial (w\boldsymbol{u})}{\partial z} = \boldsymbol{\nabla}_h \cdot \left(\nu_h \left(\boldsymbol{\nabla}_h \boldsymbol{u} + (\boldsymbol{\nabla}_h \boldsymbol{u})^T \right) \right) + \frac{\partial}{\partial z} \left(\nu \frac{\partial \boldsymbol{u}}{\partial z} \right)$$
$$- f \boldsymbol{e}_z \wedge \boldsymbol{u}' - \frac{g}{\rho_0} \int_z^{\eta} \boldsymbol{\nabla}_h \hat{\rho}(S, T) d\zeta - \boldsymbol{G}. \tag{8}$$

In practice, we omit $\boldsymbol{G}$ when solving Eq. (8). We then compute $\boldsymbol{G}$ such that $\int_{-h}^{\eta} \boldsymbol{u}' \, dz = 0$ at the end of a baroclinic iteration. This forcing term is kept constant over the barotropic iteration(s) (Eqs. (6)-(7)). A similar coupling strategy is used in Ringler et al. (2013).

2.2   Bathymetry and forcing data

The bathymetry (Figure 1) is constructed from various data sets, including ETOPO2v2 and local survey data (see Kärnä et al. (2015) for details). A minimal depth of 3 m is prescribed as wetting and drying processes are not taken into account. The methodology is the same as in MacCready et al. (2009).

The estuary is characterized by two major deep channels merging close to the mouth in a shallow estuary (see Figure 1). The North Channel is flood-dominant, the South Channel is ebb-dominant. The latter is the main driver of the freshwater discharge as shallow areas prevent the connection between the North Channel and the upstream estuary at the end of the ebb (Chawla et al., 2008).

The velocity and elevation boundary conditions are obtained by combining 13 tidal constituents of the elevation and currents from OSU TOPEX/Poseidon Global Inverse Solution TPXO7.2 dataset (Egbert and Erofeeva, 2002) with global circulation model HYCOM subtidal elevations and baroclinic velocities to construct a Flather condition on the open ocean boundaries. Open ocean boundary conditions for salinity and temperature also come from the global $1/12°$ HYCOM reanalysis (Chassignet et al., 2007). Initial values of salinity and temperature are interpolated from the HYCOM data on the shelf and vary linearly in the estuary toward in situ measurements at the upstream boundary.

The choice of the upstream limit of the computational domain, Beaver Army Terminal, comes from the availability of the river discharge and temperature collected from a USGS ADCP at this location. In summer, less than 1% of the river flow comes from downstream tributaries (MacCready et al., 2009). Water is known to be entirely fresh there.

The wind speed at 10 m above sea level and the atmospheric pressure are obtained from the NOAA/NCEP North American Mesoscale (NAM) Forecast System with a resolution of 12 km. The bulk formula from Smith and Banke (1975) is used to derive the wind stress to force the top surface boundary of the momentum equation. The heat flux is parametrized with a relaxation boundary condition toward the sea surface temperature from HYCOM and a relaxation time
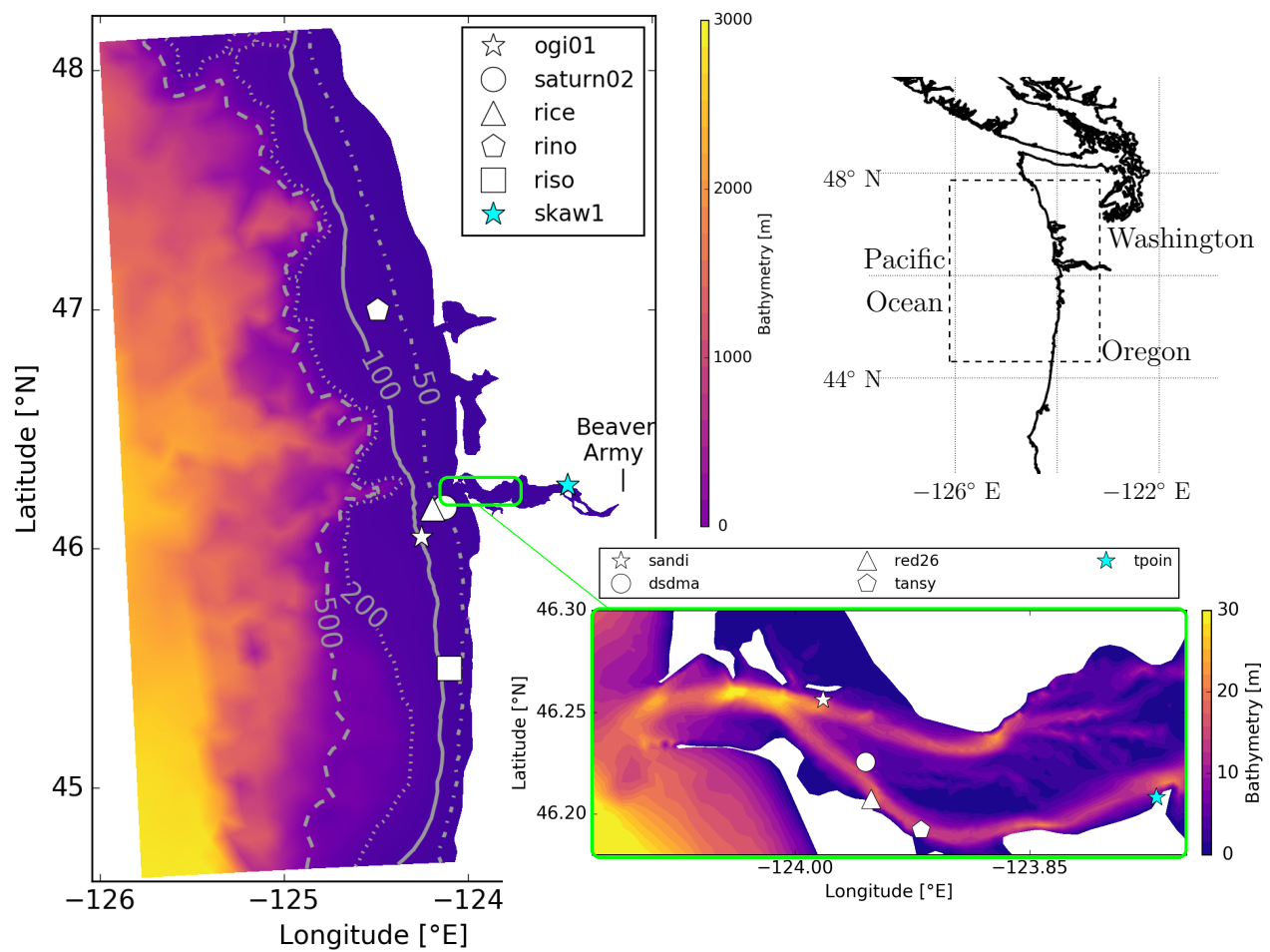
Figure 1: Computational domain colored by the bathymetry. Note the two channels merging near the mouth regulating the flow exchanges between the estuary and the ocean. Stations in white are for ADCP, and in cyan for tidal gauges.

of half a day. Evaporation and precipitation are negligible compared to the water discharge and, hence, not taken into account.

The fluvial and atmospheric conditions are represented in Figure 2. Panel (a) shows the river discharge as measured at Beaver Army terminal. The outflow is at its highest during the spring freshet period. Panel (b) of Figure 2 shows the water elevation at NOAA station located at Astoria, OR (*tpoin*) (see section 2.4 for details). The tidal signal alternates between neap and spring. Panel (c) shows the wind velocity data from NAM model at *rice* station (see Figure 1 for location). Two periods of downwelling-favorable winds (I and II) are shadowed. The impact of such conditions on the plume dynamics is studied in Section 4.

The simulation runs from April 30 until July 1 2006, and its analysis starts on May 15. As most of the estuarine water mass is flushed out in about 7 days (Kärnä and Baptista, 2016b), the analysis is performed after a two-week spin-up period.

2.3   Computational domain

The mesh spans the Columbia river-to-sea continuum, from Beaver Army Terminal located 85 km upstream of the river mouth to a distance of about 150 km offshore and 200 km alongshore in the Pacific ocean (Figure 3).

The 3D mesh is created in two steps: a 2D unstructured horizontal mesh is first generated for the whole $z = 0$ surface with GMSH (Geuzaine and Remacle, 2009); each triangle is then vertically extruded to obtain a 3D mesh made up of prisms. The mesh is structured in the z direction where all lateral facets are strictly vertical.

The 2D mesh is made up of 1.22×10^4 elements with a resolution ranging from 400 m to 10 km, with the finer mesh located in the estuary and a smooth transition from fine resolution near the coast to a coarser resolution in the open ocean (Figure 3). The use of unstructured meshes provides tools to include both small-scale estuarine processes and large-scale shelf circulation within a single model with neither nudging nor nesting.

For the vertical extrusion, there are three major types of vertical grids: staircase-like z, terrain-following or isopycnal coordinates. Terrain-following coordinates precisely follow the exact bathymetry, but need a uniform number of vertical cells over the domain (or the connection of one prism with two others) and suffer from a lack of resolution near the surface. They also introduce internal pressure gradients errors (Haney, 1991). With z-coordinates, the problems are inverted: the bathymetry is poorly represented unless a very large number of layers is used but no specific treatment is needed for the pressure gradient. In order to benefit from both discretization, SLIM 3D allows for the use of hybrid grids: terrain-following for shallow regions to correctly represent the bathymetry, and staircase below for deeper areas to avoid pressure gradient related errors. The mesh is constructed such that Haney's hydrostatic consistency criterion is satisfied for all truncated elements (Haney, 1991).

In the present CR benchmark, the vertical extrusion of the 2D mesh is done over 8 terrain following levels in shallow regions (depth < 150 m, see top right panels in Figure 3). To increase the near-surface resolution, the depth of each level is saturated, as a maximal thickness is prescribed for each layer (layers are located, at most, 0.5, 1, 3, 5, 12, 30, 60 and 150 meters
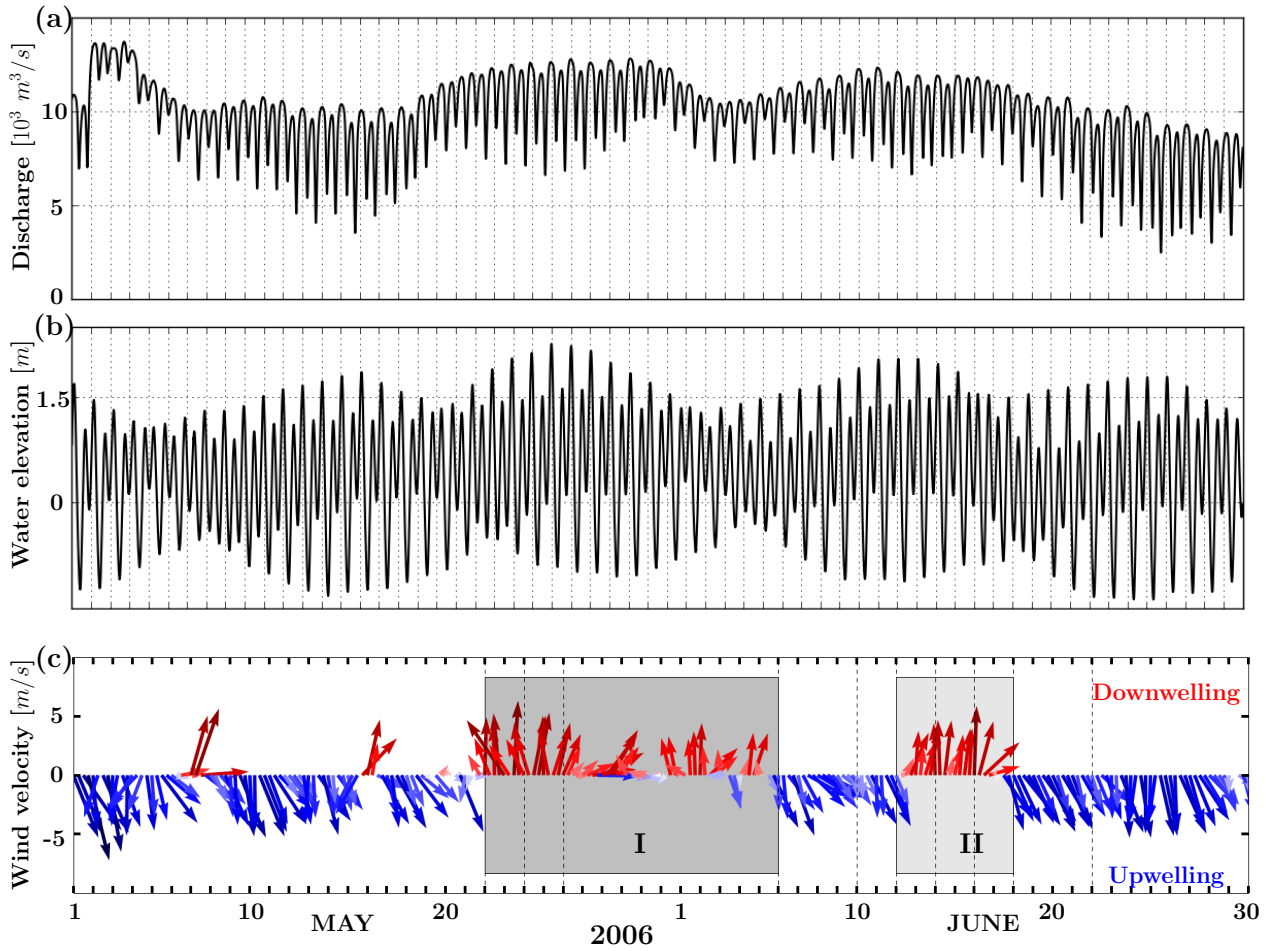
Figure 2: Timeseries of the fluvial and atmospheric conditions for the simulated period: (a) the river discharge measured at Beaver Army, (b) the water elevation observed at station *tpoin*, and (c) the wind velocity from the NCEP-NAM model at station *rice*. Shadowed areas denoted I and II are the downwelling-favorable wind periods considered in Section 4.
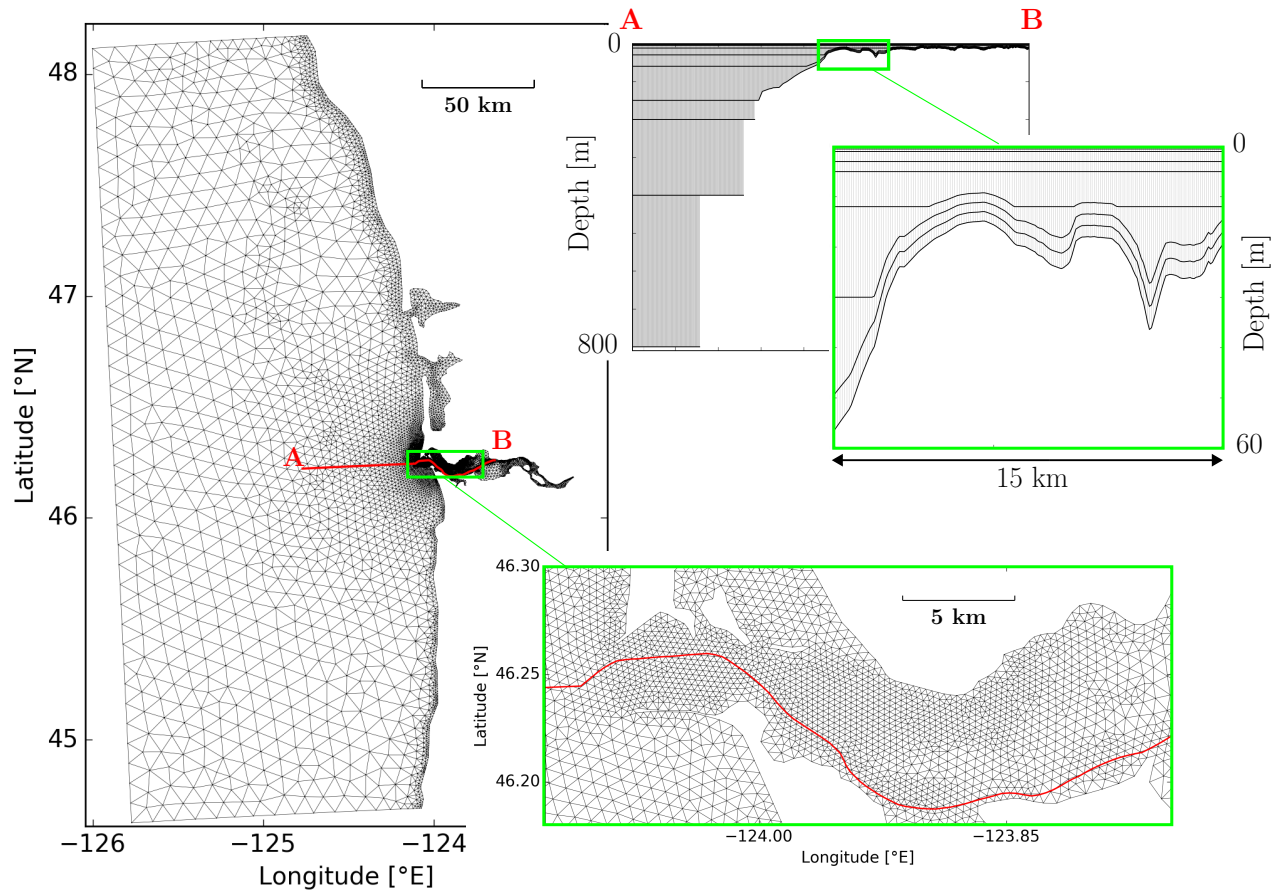
Figure 3: Computational domain: top view of the unstructured 2D mesh (1.22×10^4 triangles). The horizontal grid resolution is increased close to the coastlines, and further increased in the estuary (see bottom right). The resolution ranges from about 400 m to 10 km. The vertical mesh along the AB transect (red curve) is shown on the top right panels. The hybrid grid consists of a mix of z and terrain-following coordinates.

below the surface). Below those layers, up to 7 z layers are added to fit the bathymetry (at 250, 400, 800, 1200, 1700, 2300, 3000 meters below surface). The whole grid is made up of about 10^5 prismatic elements.

2.4   In-situ observations

Time series of water elevation are collected at the following National Oceanic and Atmospheric Administration (NOAA) tidal gauges: Astoria, Tongue Point, OR (*tpoin*), located in the South Channel, and Skamokawa, WA (*skaw1*), located upstream in the River. Tidal gauges are high-lighted in cyan in Figure 1. Time series of salinity and temperature are collected at stations from the SATURN network managed by the Center for Coastal Margin Observation and Prediction (Baptista et al., 2015). The analysis of salinity and temperature is performed at 4 SATURN stations in the estuary: *dsdma* (7.3 m), *sandi* (7.9 m), *red26* (7.5 m) and *tansy* (8.4 m); and 2 on the shelf: *ogi01* (0.8, 5, 11 and 50 m) and *saturn02* (1, 5 and 17 m)

Three moorings were deployed on the shelf close to the CR mouth during the RISE (River Influence on Shelf Ecosystem) project (see Hickey et al. (2010) and references therein). All moorings are located on the 72 m isobath: *rice* off the river mouth, *rino* about 100 km North of the mouth, and *riso* about 70 km South (see Figure 1). Temperature and salinity are recorded at several depths (1 and 20 m for all, and 5 m only for *rice*).

The pointwise plume depth is computed at two locations to compare with observations: *ogi01*, a buoy from the SATURN observation network located along the 100 m isobath, 30 km southwest of the CR mouth, and *saturn02*, a SATURN endurance station, located just down-stream the river mouth. The plume profile over the depth is obtained by linearly interpolating the data over the vertical. The plume depth is the part above the 26 ‰ isohaline.

2.5   Error metrics

The quantitative assessment of the model skill is similar to Kärnä and Baptista (2016a). In-tuitive metrics, such as bias and root mean square error (RMSE), have the same units as the variable, and hence facilitate the interpretation of the results. The RMSE still suffers from the presence of outliers and is scale-dependent. In order to compare metrics between variables at different scales, an additional metric is computed, the normalized root mean square error (NMSE). The latter is zero for a perfect model, one for a model with an error equal to the observed variability, and greater than one for models that yield an error larger than observed variability. The definition is similar to the Murphy (1988) score if the mean of the observations is taken as the reference.

The model skill can be summarized by drawing normalized Taylor diagrams (Taylor, 2001), where the radial coordinate is the model standard deviation, normalized by the standard deviation of the observations (NSD), and the angular coordinate is arccos($Corr$) with $Corr$ the Pearson correlation coefficient. On this diagram, the normalized centered root mean square (NCRMSE) appears as a radial distance from the position of a perfect model (radius = 1, angle = 0). The metrics we consider are defined as follows:

$$\text{Bias} = \bar{m} - \bar{o},$$

$$\text{RMSE} = \sqrt{\frac{1}{N} \sum_{i=1}^{N} (o_i - m_i)^2},$$

$$\text{NCRMSE} = \sqrt{\frac{1}{N} \frac{1}{\sigma_o^2} \sum_{i=1}^{N} ((m_i - \bar{m}) - (o_i - \bar{o}))^2},$$

$$\text{NMSE} = \frac{(\text{RMSE})^2}{\sigma_o^2},$$

$$\text{NSD} = \sqrt{\frac{1}{N} \frac{1}{\sigma_o^2} \sum_{i=1}^{N} (m_i - \bar{m})^2},$$

$$\text{Corr} = \frac{\sum_{i=1}^{N} (o_i - \bar{o})(m_i - \bar{m})}{\sqrt{\sum_{i=1}^{N} (o_i - \bar{o})^2} \sqrt{\sum_{i=1}^{N} (m_i - \bar{m})^2}},$$

where o_i and m_i are the observed and modeled values at time step i, respectively, and $\bar{y}$ and σ_y^2 stand for the mean and variance of y. As the Taylor diagram is based on centered signals, the analysis is complemented with a BIAS-NMSE plot. The error metrics are also computed for *db33*, the most recent longterm hindcast database output from SELFE (Kärnä et al., 2015).

2.6   Plume metrics

Understanding the space-time evolution of the plume can be difficult as its 3D shape rapidly changes with wind conditions. We therefore consider the metric of Burla et al. (2010) to easily visualize the global plume dynamics. By integrating the 3D salinity field over space, we generate time series for the volume, surface area, thickness and centroid location of the plume. Following Horner-Devine et al. (2009), the $S_t = 26$ ‰ salinity threshold delimiting the re-circulating plume from the far-field plume is chosen for these definitions. This cutoff is sufficiently small to differentiate the CR plume from ocean waters and other freshwater sources. The estuaries are not taken into account for the plume metrics.

The plume area defines the ocean water surface with a salinity below S_t. In the same sense, we define the plume volume as the sum of the volumes of each prism which mean salinity is below the threshold. The mean plume thickness is simply the ratio of the plume volume to its area. In addition to the latter thickness, the depth of the plume is assessed at stations *ogi01* and *saturn02*.

Tracking the location of the plume can be assessed by computing the surface plume centroid. This is the area-weighted mean of the center of each surface plume triangle:

$$\vec{x}_s = \frac{\displaystyle\int_{S \leq S_t} \vec{x} d\Gamma}{\displaystyle\int_{S \leq S_t} d\Gamma},$$

where Γ is the top surface of the computational domain and $\vec{x}$ is the position vector of the center of each triangle.

This metric cannot show the occurrence of a bidirectional plume, as it is only a single point, but may give an idea of the predominance of one plume direction to the other.

3 Model validation

The error metrics defined in Section 2 are used to evaluate the model skill for the elevation, salinity and temperature. The validation distinguishes between estuary and shelf stations.

The salinity intrusion in the estuary is caused by both tidal pumping and gravitational circulation (Chawla et al., 2008). During floods, tidal straining brings salty water in the estuary channels (de Boer et al., 2008). Major ebb currents then flush most of the salinity downstream, while minor ebb currents allow for salinity retention. The top layer of the river remains relatively fresh at all times, even during major flood tides, as freshwater outflow still drives the top of each water column. In numerical models, the salinity retention and gravitational circulation are often underestimated due the challenging complexity of the area, especially during neap tides (Kärnä and Baptista, 2016a). In this section, we first validate SLIM 3D simulations in the estuary using the indicators defined in Section 3.1.

The spatial evolution of the CR plume can exhibit a strong variability at time scales of a few days (see Northward wind periods I and II in Fig. 2), largely driven by changes in wind direction (Hickey et al., 1998; Liu et al., 2009a; Burla et al., 2010). Shorter wind fluctuations over just one day are also observed (e.g. on May 8th and 16th in Fig. 2) but have a weaker impact on the plume. Those fluctuations can be strong in late spring and early summer. The CR plume is strongly affected by these changes as Ekman transport dominates the dynamics of the upper layer of the coastal ocean. The ability of SLIM 3D to capture the plume dynamics is assessed by means of comparison with in-situ observations in Section 3.2.

A comparison to existing model of the coupled CR estuary-plume using ROMS and SELFE is also performed. ROMS results come from the RISE project (MacCready et al., 2009; Liu et al., 2009b), and SELFE results are extracted from the most recent longterm database called *db33* (Kärnä et al., 2015). The comparison is not direct as settings and forcings are not the same in all models. We list here major differences between those models. Both domains covered by SELFE and ROMS spread over a larger part of the Pacific ocean. SELFE and ROMS are nudged toward global Navy Coastal Ocean Model (NCOM), whereas SLIM 3D is forced only at the boundaries with HYCOM model outputs. ROMS and SELFE use bulk formula to compute heat fluxes whereas a relaxation to the SST is used in SLIM 3D. Horizontal spatial resolution in the plume region ranges between 1 and 10 km for SLIM 3D, between 200 m and 2 km
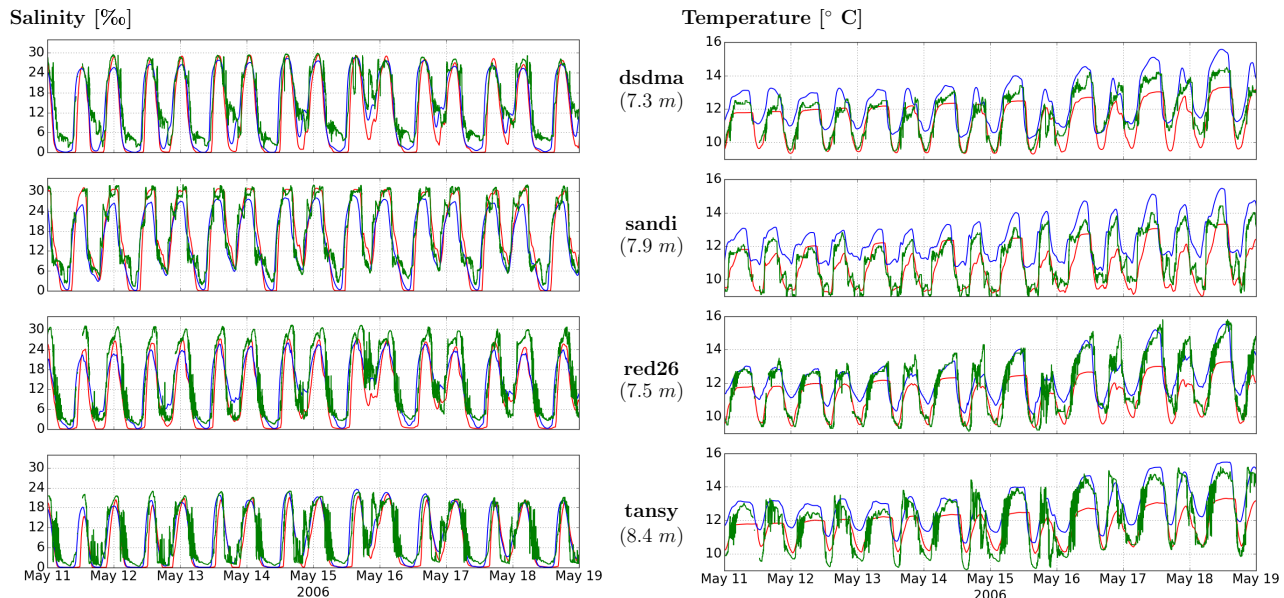
Figure 4: Comparison of salinity and temperature at different stations in the estuary. The depth of measurement is shown below the stations name (see Fig. 1 for the stations location). Each panel compares SLIM 3D model outputs (red), measurements (green) and SELFE results (blue) at stations *dsdma*, *sandi*, *red26* and *tansy*. The major characteristics of the salinity evolution in the estuary are well reproduced by the model close to the mouth. Compared to SELFE, SLIM 3D better captures the flood peaks of salinity, but slightly underestimates salinity levels during ebbs

for SELFE and 400 m for ROMS. In the vertical direction, ROMS and SELFE both use S coordinates (Haidvogel et al., 2000). There are 20 levels in ROMS and 37 levels in SELFE, 17 z-levels are added below 100 m in the latter. By comparison, SLIM 3D only use 8 terrain-following cells and 7 z-levels below 150 m. Despite the lower resolution, the low-order heat flux parametrization, and the absence of relaxation to the external global model, we investigate how well SLIM 3D compares with the other two models.

3.1   Estuarine dynamics validation

The dominant tidal features in the estuary are well reproduced by the model. As shown in Figure 4, the model skill at *sandi* station proves the good representation of the flow exchanges between the estuary and the shelf. All stations show that the peaks of salinity intrusion during flood tides are well captured by the model. The ebb flushing is somewhat overestimated as the predicted salinity is slightly below observations (Figure 4).

Figure 5 summarizes the values of several error metrics for water levels, temperature and salinity at different estuarine stations on a Taylor diagram and a NMSE versus normalized bias plot. All skill metrics are listed in Table 1. SLIM 3D represents well the elevation in the
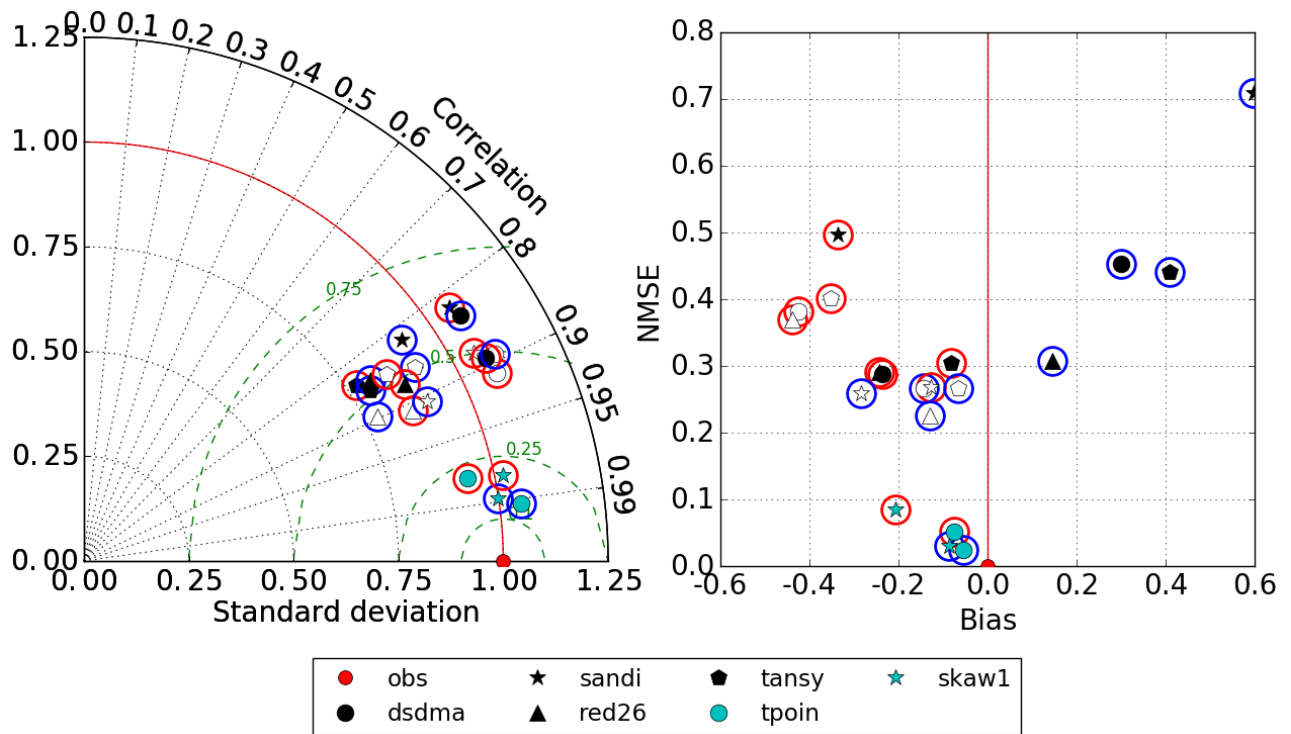
Figure 5: Normalized Taylor diagram (left) and NMSE versus normalized bias (right) for SLIM 3D (red circles) and SELFE (blue circles) models outputs in the estuary. The colors of the markers indicate the variable: white is salinity, black is temperature and cyan is elevation. In the Taylor diagram, normalized standard deviation is on the radial axis; correlation coefficient is on the angular axis; green dashed lines indicate NCRMSE. The bias is normalized by the standard deviation of the observations. SLIM 3D skill is very high for elevation and high for salinity and temperature. The skill is comparable to the one obtained with SELFE.

estuary and achieves a NMSE of less than 0.1. The overall correlation is close to 1 (0.98). All data points fall within the 0.25 NCRMSE circle. This good model skill is comparable to that of SELFE.

The model reproduces the bottom salinity and temperature evolutions with good skill at all stations, with a RMSE of about 5 ‰ for the salinity and about 1° C for the temperature (not shown). The NMSE is small for both variables, between 0.27 and 0.48. Correlations are also high, with a minimal value of 0.82. All stations are located close to the river mouth and in the south channel. Producing a good performance there confirms that SLIM 3D is well suited to represent the exchanges between the river and the ocean.

Compared to SELFE, we obtain slightly higher bias and NMSE for the salinity. Skill metrics for temperature are better with SLIM 3D than SELFE. In the estuary, SLIM 3D also achieves slightly better skill than ROMS (salinity correlations of 0.91 vs 0.88 at *dsdma*, 0.91 vs 0.90 at *red26*, 0.88 vs 0.84 at *sandi*, see Liu et al. (2009b) for details), even though the metrics are not directly comparable as the simulated time periods are different.

3.2   Plume dynamics validation

In order to assess the quality of the simulations over the shelf, the salinity signal observed at RISE stations is compared to model results. Figure 6 shows that SLIM 3D simulations (solid lines) represent all the major events recorded in the observations (dotted lines). At northern station *rino*, the two major brackish water events recorded around June 7 and June 19 are well reproduced by the model. Predicted values slightly overestimate freshness at the surface (red, 1 m depth) during the first event and underestimate the second one by only 10%. Interestingly, the plume signature is not visible at *rino* when wind is downwelling-favorable (northward), although the plume is spreading to the North. The plume spreads shoreward of the mooring, and is thinner than the inner shelf delimited by the 72 m isobath. The decrease in salinity is observed a few days after wind reversals, as the plume detaches from the Washington coast and reaches the station. SLIM 3D proves capable of capturing this upwelling-induced detachment, even though the decrease in salinity is less sharp. By comparison, SELFE response to the event starts earlier and the amplitude is less intense. The major event around June 15 observed at the southern station *riso* is also well captured, in terms of the amplitude and the duration, while SLIM 3D predictions show a one-day time lag. At *rice*, the station close to the river mouth, the signal variability is stronger because it is influenced by the near-field tidal plume. The model correctly represents the stratification for most of the period under consideration. The absence of brackish water at the end of May is well reproduced, although the model predicts a non-recorded brackish water event at the beginning of June. On the bottom panel of Figure 6, a closer view of salinity at *rice* confirms that SLIM 3D can predict the amplitude of tidal-induced oscillations of the salinity as well as slower changes.

In Figure 7 and 8, skill metrics of SLIM 3D are detailed with red circles on a Taylor diagram and a plot of the NMSE versus the bias. All skill metrics are listed in Table 2. For salinity, the biases and RMSE are small, except at 1 meter depth where the variability is strong. Almost all NMSE are below 1 (Figure 7, red circles). This proves that SLIM 3D errors are below the
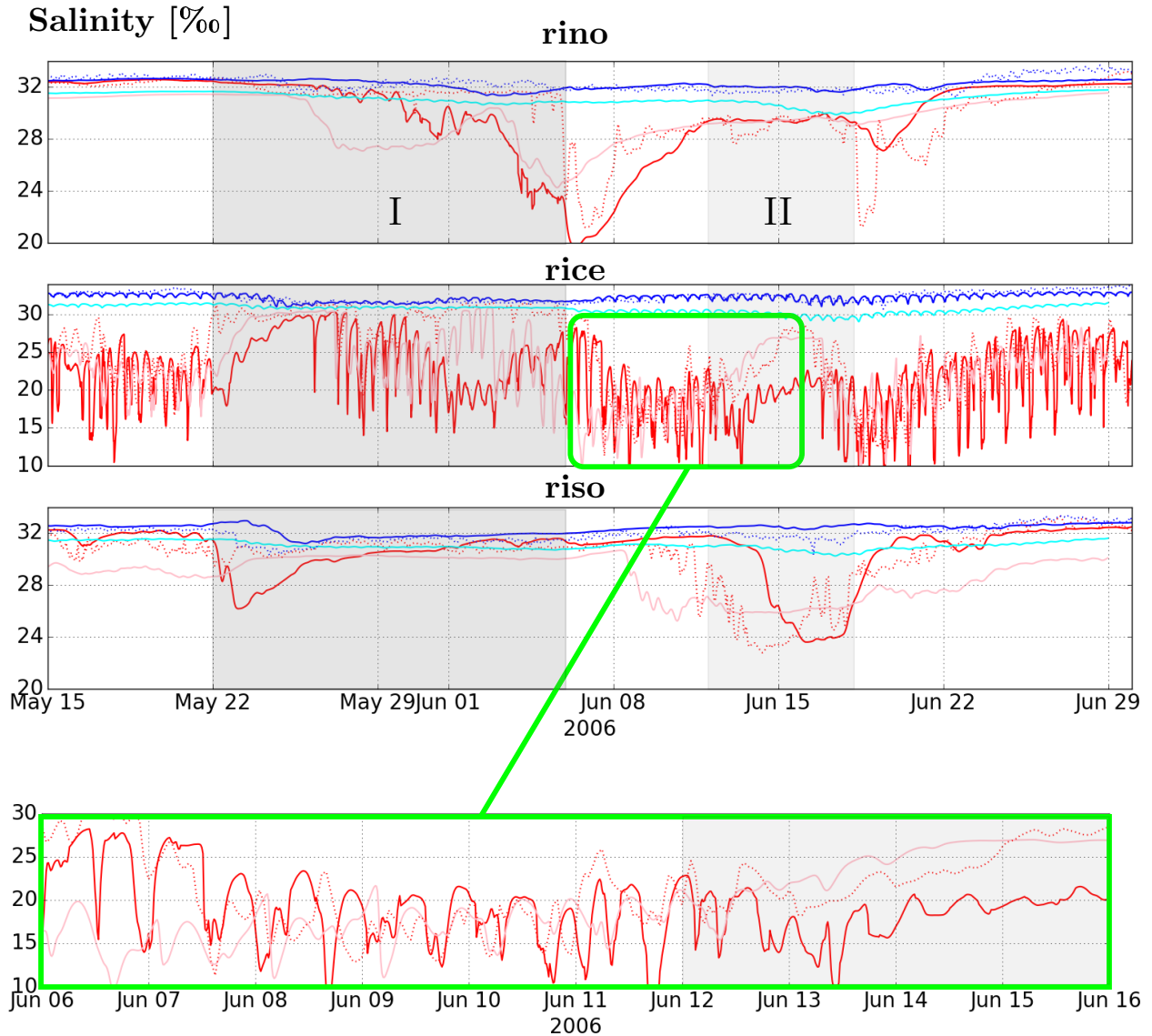
17

Figure 6: Observed (dotted line) and modeled (solid line) time series of salinity at RISE stations (see locations in Fig. 1) at 1 m (red) and 20 m (blue) below the sea surface. SELFE model outputs are shown for comparison in pink and cyan, respectively. The bottom panel is a close-up view on the *rice* station. Roman numerals and shadowed periods refer to the downwelling periods shown in Figure 2. The model reproduces the major events at *rino* and *riso*. At *rice*, both the model range and the variability agree well with the observations of the bulge, as confirmed by the zoom-in view.
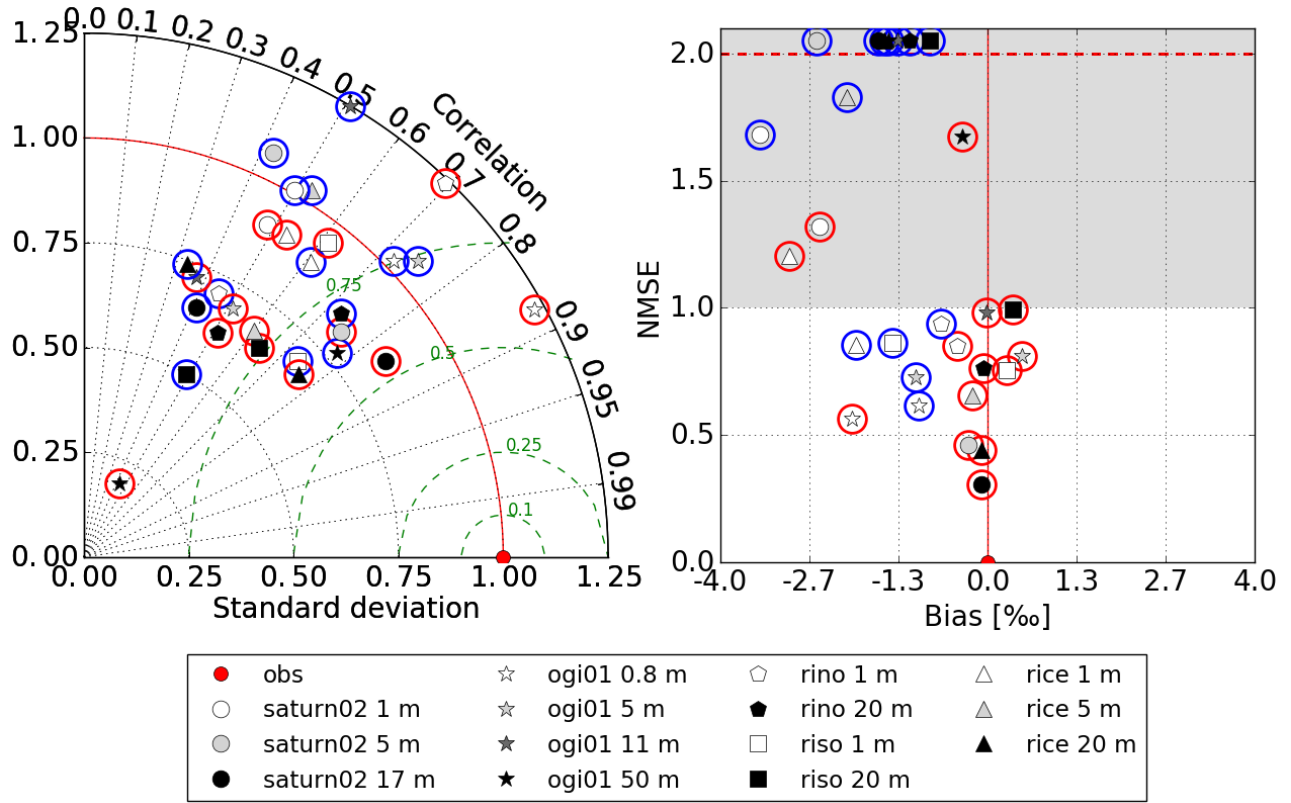
Figure 7: Normalized Taylor diagram (left) and NMSE versus bias (right) for SLIM 3D (red circles) and SELFE (blue circles) models outputs on the shelf for salinity. The grayscale of the markers indicate the depth: white is shallower, dark is deeper. In the Taylor diagram, normalized standard deviation is on the radial axis; correlation coefficient is on the angular axis; green dashed lines indicate NCRMSE. On the right panel, NMSE larger than 2 are placed just above the red dashed line irrespective of their values (see Table 2 for exact values). SLIM 3D skill is in general better than SELFE in terms of biases, NMSE and correlations.
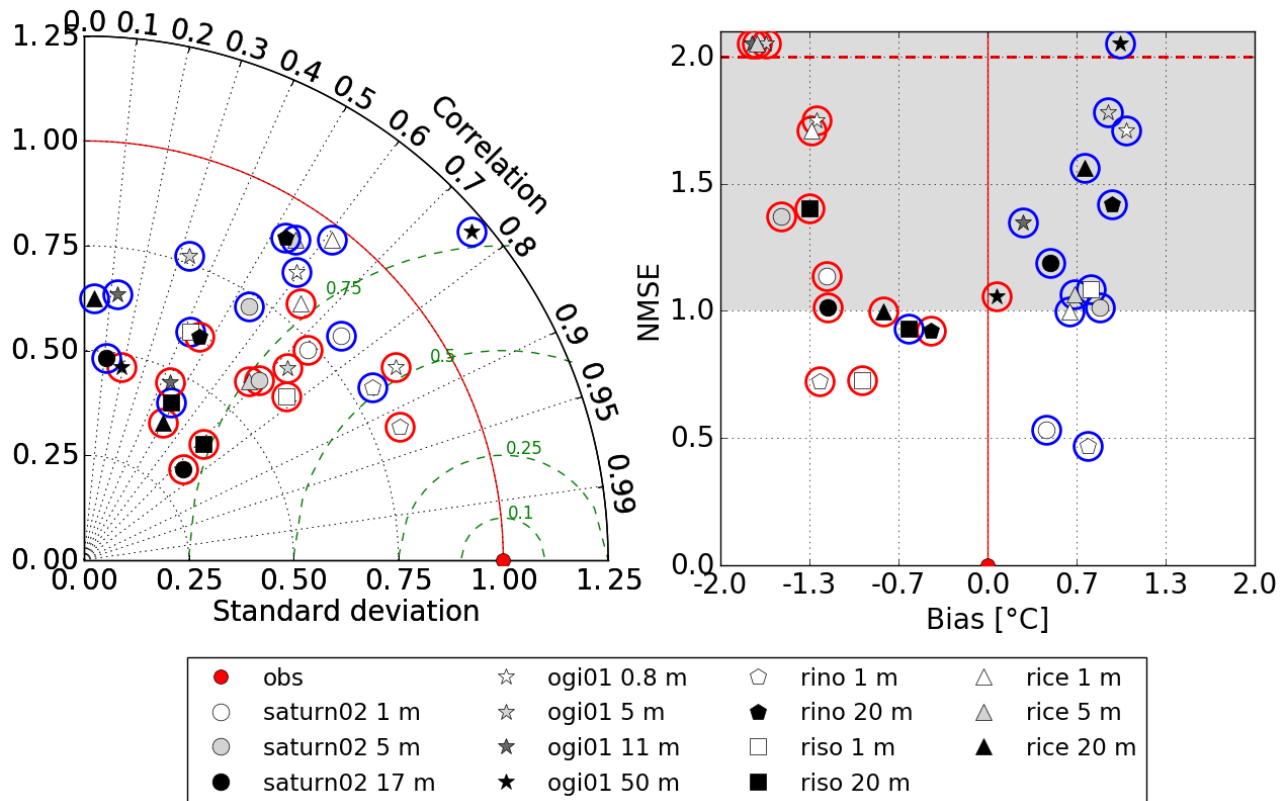
Figure 8: Normalized Taylor diagram (left) and NMSE versus bias (right) for SLIM 3D (red circles) and SELFE (blue circles) models outputs on the shelf for temperature. The grayscale of the markers indicate the depth: white is shallower, dark is deeper. In the Taylor diagram, normalized standard deviation is on the radial axis; correlation coefficient is on the angular axis; green dashed lines indicate NCRMSE. On the right panel, NMSE larger than 2 are placed just above the red dashed line irrespective of their values (see Table 2 for exact values). SLIM 3D skill is in general better than SELFE in terms of correlations and NCRMSE, but slightly worse in terms of biases.

variability of the measurements. For temperature, SLIM 3D skill is good, but all stations seem to underestimate the temperature (Figure 8, red circles), as opposed to SELFE that has almost only positive biases.

Burla et al. (2010) reported poor correlation between modeled and observed salinities at *rice* station, due to the inability of SELFE to reproduce the small scale variability in the bulge. The metrics shown in Figure 7 (blue circles) prove that SELFE skill on the shelf has strongly improved with *db33* (Kärnä et al., 2015). A direct comparison of skill metrics shows that SLIM 3D has a better skill on the shelf in predicting the salinity. Biases and NMSE are smaller at almost every stations and depths. SELFE predictions seem to underestimate salinity at every station. The comparison for the temperature is favorable to SELFE in term of bias, but the NMSE are comparable and correlations favor SLIM 3D. The maximal value of NMSE of SLIM 3D is 2.48 for temperature and 1.69 for salinity. By comparison, SELFE *db33* NMSE exceed these values at several stations and depths, with worse values at *ogi01* 50 m (12.96 for salinity, 4.57 for temperature). Only a single value of correlation obtained with SLIM 3D is below 0.42 (0.22 for temperature at *ogi01* 50 m deep). Several correlations obtained with SELFE lie below this value, with even a value close to 0 (0.04 for temperature at *rice* 20 m deep).

The plume thickness estimation at station *ogi01* and *saturn02* is obtained by linearly interpolating the measurements at recorded depths (0.8, 5, 11 and 50 m for *ogi01* and 1, 5 and 20 m for *saturn02*). The 26 ‰ salinity threshold time series are scattered against the simulated values in Figure 9. At *ogi01*, the absence of the plume at the end of May and at the beginning of June is well represented by the model. The time of appearance (06/08) also matches the observations. Predicted thickness slightly differs. The model misses the disappearance of the plume around mid-June. The predicted salinity remains just below the 26 ‰ salinity threshold defined in Section 2.6, although the observed data are just above this value. The onset and vanishing plumes at this station are correctly estimated by the model at the end of June. At *saturn02*, correlation between predicted and observed plume thickness is stronger. The thickness grows around mid-June, and drops after June 20. At a smaller time scale, the tidal amplitude is also correctly predicted.

4 Model application: wind-induced variability of the plume

The CR plume dynamics is characterized by two major regimes. In winter, the freshwater flow leaving the CR estuary turns North due to the Earth's rotation, reinforced by downwelling-favorable winds, generating a thin plume attached to the Washington coast. In summer, as the wind strongly blows southward due to the predominance of a high pressure anticyclone, the plume is oriented in an offshore south-west direction. During spring-summer, the CR plume is known to be regularly split into two parts. In this section, we investigate the response of the plume to wind changes.

The wind direction is mostly southward during late spring and summer in the North-East
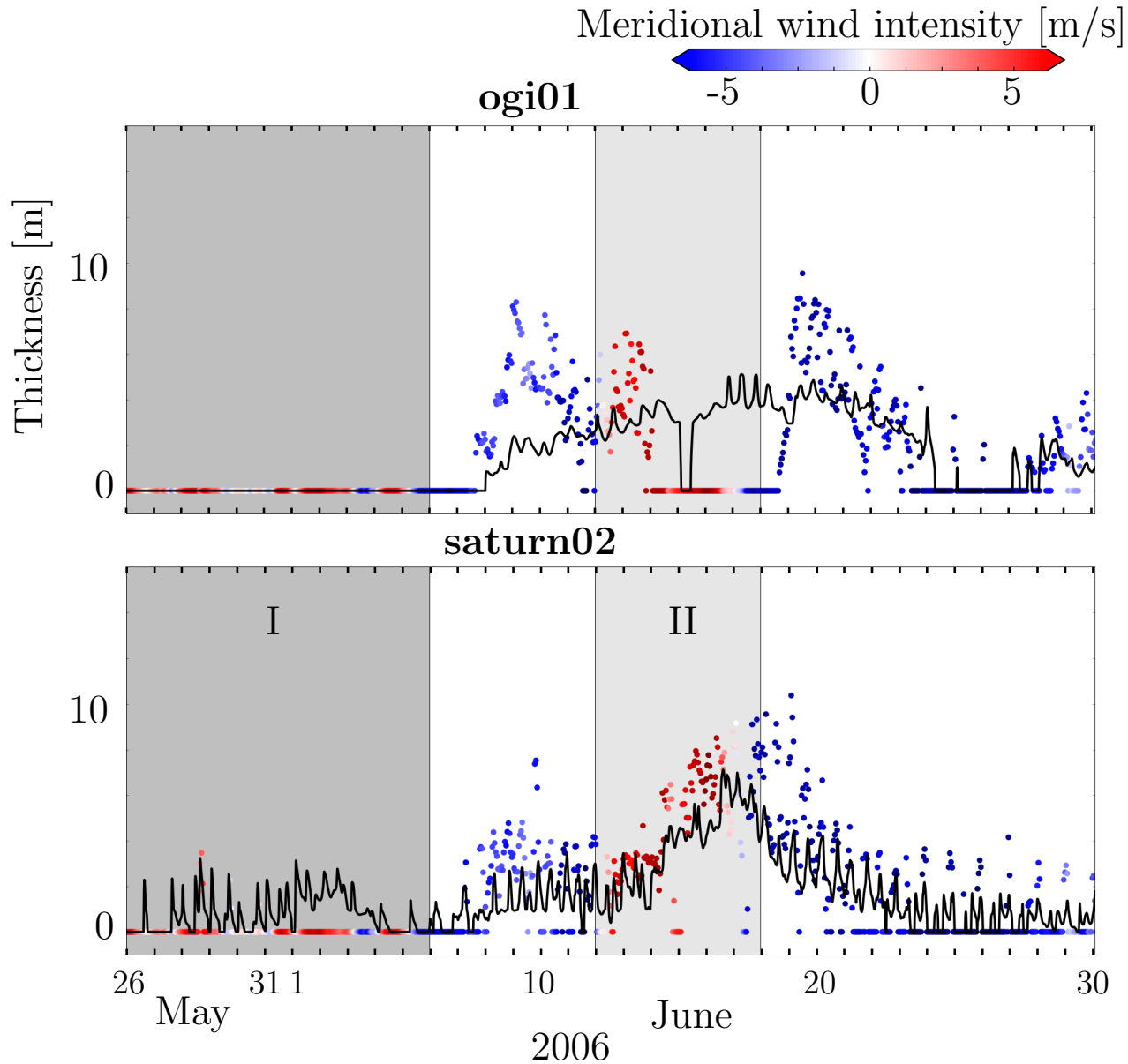
Figure 9: Time series of the thickness of the plume at *ogi01* and *saturn02* as predicted by SLIM 3D (black line) compared to the observations (dots). The dots are colored by vertical wind speed intensity and direction: red for a northward wind, blue for a southward wind. While no brackish water is recorded nor predicted at *ogi01* before June 8, SLIM 3D captures the appearance of the plume afterwards, while underestimating its size. Correlation is strong at all times, except when the plume vanished between June 14 and June 18, which SLIM 3D partly failed to capture. Short plume appearances at the end of June are well reproduced. At *saturn02*, except between May 30 and June 6, the plume appearances and sizes are well predicted by the model.
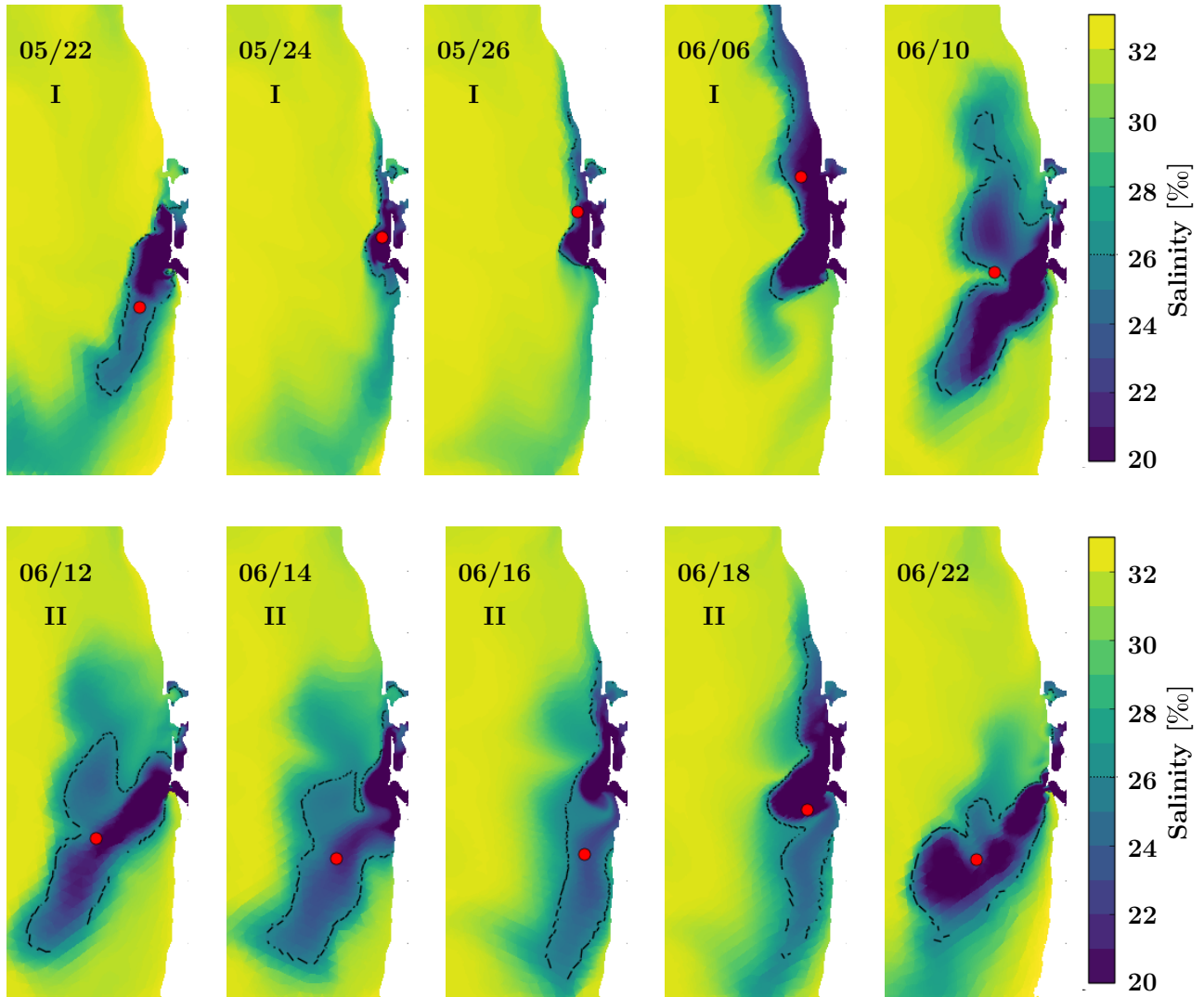
Figure 10: Instantaneous surface salinity from SLIM 3D simulations. The dotted lines represent the 26 ‰ iso-salinity and the red dots indicate the plume centroid. The top panels exhibit a plume dynamics similar as the conceptual model described in Hickey et al. (2005). The bottom panels show that a shorter downwelling-favorable event may not be strong enough to erode the plume along the Oregon coast. Note the longer period between the third and fourth panels in the top row than in the bottom row. See Figure 2 for details about the wind.

Pacific region. Short wind reversals regularly happen, interrupting the well-established atmospheric conditions. As shown in Figure 2, the period May-June 2006 is no exception, as the wind mainly blows southward, with short and long wind directional shifts. For example, wind shifts lasting less than a day happen around May 8 and May 16, while the period between May 21 to June 6 is almost continuously downwelling-favorable. The year 2006 is characterized by early spring transition, large river discharge and early freshet.

Hickey et al. (2005) defined a data-derived conceptual model of the bidirectional summer plume, which is clearly depicted by the top panels of Figure 10 describing the first downwelling event (I). The wide CR far-field plume extends offshore in a South-West direction as upwelling-favorable winds blow strong (05/22). After about 2 days of downwelling-favorable wind (05/24), the aged plume is driven toward the coast, and a new plume emerges North of the river mouth. The bulge turns North generating an along-coast plume and the southerly plume is almost fully eroded within 4 days (05/26). The downwelling-favorable winds constrict the plume along the Washington coast but, after several days and as wind intensity declines, the plume starts widening (06/06). As soon as the wind blows from the North again, the along-coast plume detaches (06/10) and nearly vanishes (06/12), soon afterwards. This plume evolution is in agreement with the conceptual model of Hickey et al. (2005)

The bottom panels of Figure 10 describe the second downwelling event (II). The far-field plume again extends in its summer-common south-west direction, made up of a majority of primarily aged water originating from the plume along the Washington coast (06/12). The wind regime once more changes and pushes the far-field plume onshore and the bulge northward (06/16). The bulge quickly responds to form a Coriolis-driven near-field plume (06/14). This downwelling-favorable event is not strong enough to fully erode the southern plume, hence both the Oregon and Washington coasts are connected to a brackish water plume (06/18). The southwest plume after period II is a combination of aged plume waters from Oregon coast, medium-aged plume waters from Washington coast and new plume waters directly coming from the river mouth (06/22). The model snapshots show that, unlike the conceptual model by Hickey et al. (2005), significant downwelling events may not be sufficient to fully erode the southern plume waters during late spring / early summer. Both duration and intensity of the event impact the plume erosion on the Oregon shelf.

In the literature SELFE has been shown to produce similar patterns in the plume dynamics (Hickey et al., 2009). Figure 11 shows a comparison of the surface salinity predicted by three models of the CR estuary and shelf: ROMS (MacCready et al., 2009; Liu et al., 2009b), SLIM 3D and SELFE (Kärnä et al., 2015). Despite a coarser vertical and horizontal resolution, SLIM 3D shows more lateral structures than SELFE, where fronts and gradients are smoothed out. While the plume extensions predicted by all models are rather similar, a major difference between simulations is the detachment from the Washington coast on June 9 that is well captured by SLIM 3D and ROMS, and not by SELFE. This detachment is a consequence of coastal upwelling, which is correctly represented with SLIM 3D. As forcings differ between models, part of the differences is not directly related to the numerics of the model.

As explained in Section 2, the plume centroid is defined as the geographic center of the plume. Its location is a good proxy for interpreting global movements of the CR plume. Figure
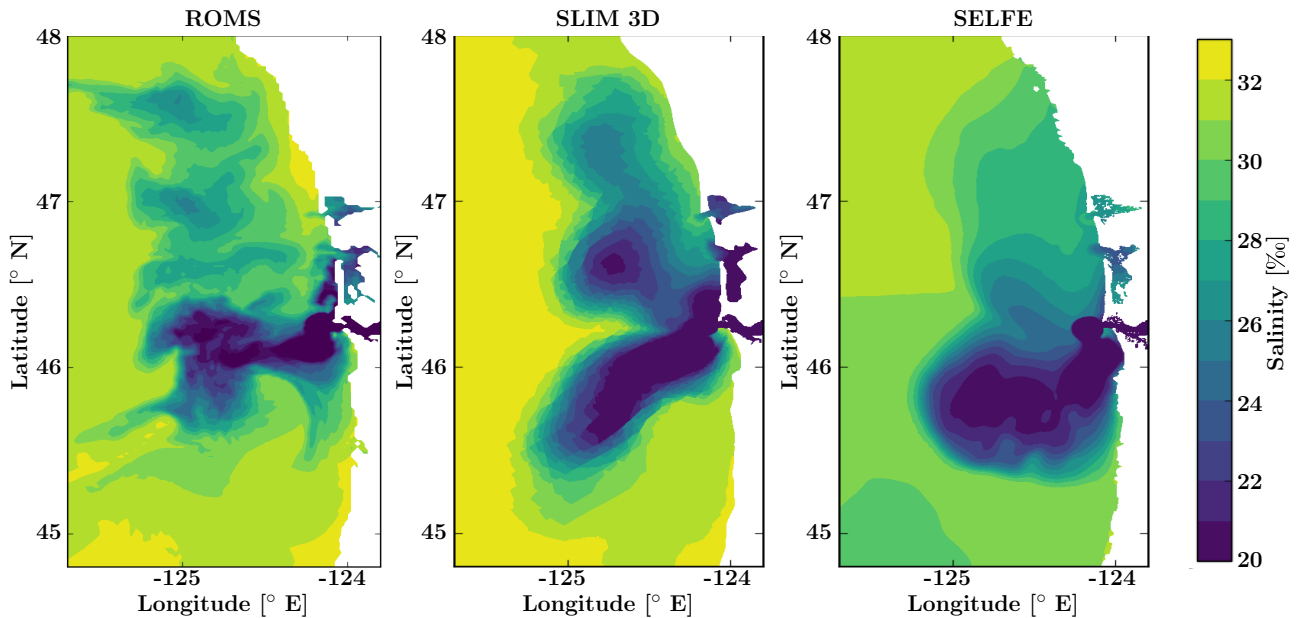
Figure 11: Instantaneous sea surface salinity simulated by ROMS, SLIM 3D and SELFE (*db33*) for June 9 2006 04:00 (PST). The bidirectional plume is well captured in all models. Note the differences in the direction of the southward propagating new plume and in the representation of the aged plume off the Washington coast.

12 displays the 2D plume centroid colored by the plume thickness, as defined in Section 2. As expected for this season, the plume location is mainly South-West of the river mouth, at an average distance of about 80 km (Figure 12).

During the first three weeks of May, the plume centroid mainly lies southwest of the CR mouth. This feature is only modified by limited strong-downwelling events, slightly moving it North-East. The plume experiences a long excursion to the North between May 22 and June 12 (Figure 12). The first part of this period is characterized by strong downwelling-favorable winds (Figure 2, period I) which drives the plume northward. The course of events is as follows: first, the plume quickly moves shoreward to reach the coast; then, it slowly continues up along the Washington coast as long as winds favor downwelling; after that, as downwelling-favorable wind intensity diminishes at the beginning of June during a storm, the plume centroid moves West but remains off the Washington shelf; finally, as upwelling-favorable winds take over again, the plume slowly moves southward and comes back to a position South-West of the CR mouth, further away than before the event. Similar patterns of atmospheric conditions occurred between June 12 and June 18 (Figure 10). The plume as estimated by the plume centroid location reacts less intensely: a similar loop as the one described earlier is visible, but the distance traveled is far smaller. The centroid starts further away from the coast at the start of the event. This means that the plume spreads over a larger area of the shelf. A criterion based on this distance and the northward wind intensity may be defined to predict the full erosion of the plume off the Oregon shelf, as predicted by Hickey et al. (2005).
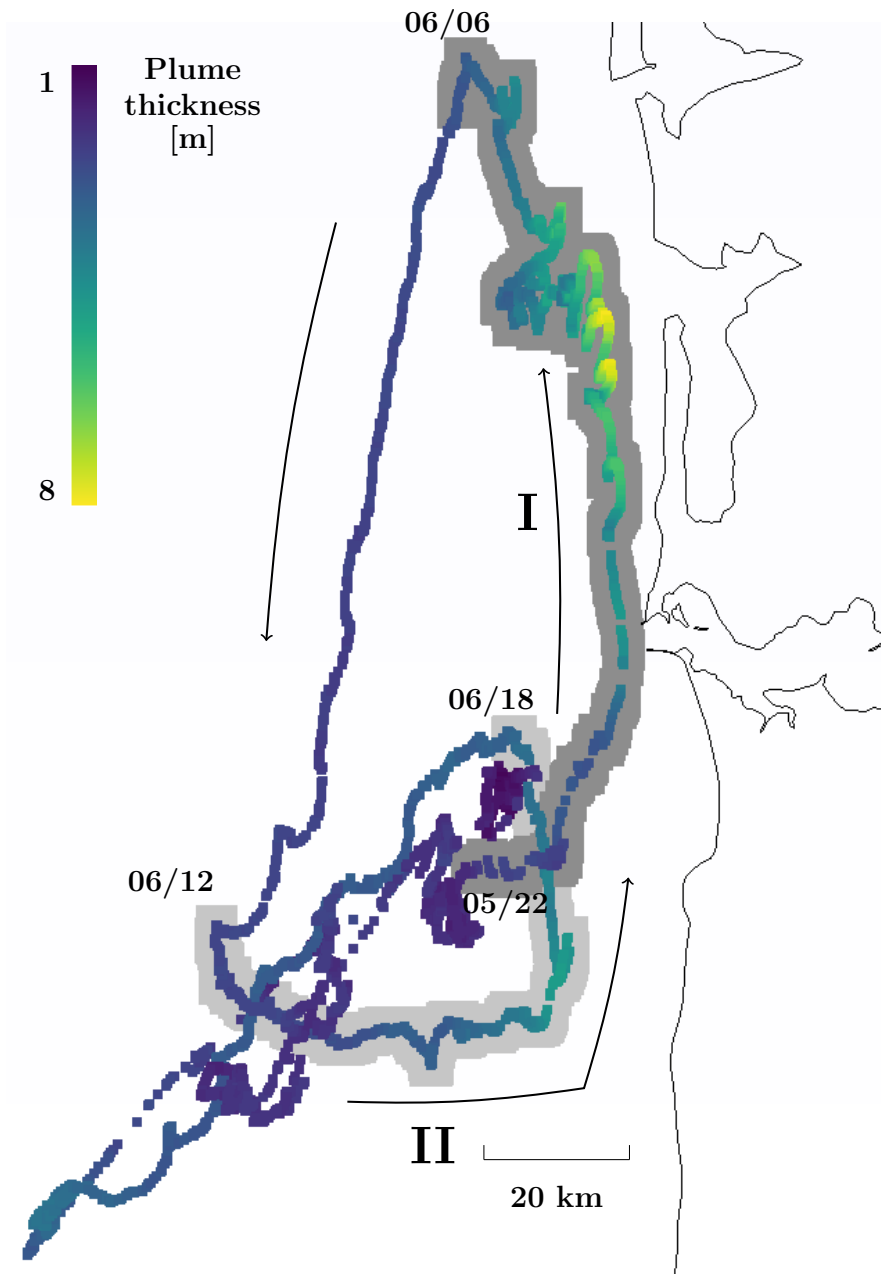
Figure 12: Position of the surface plume centroid every 15 minutes with color referring to the thickness of the plume. Roman numerals and grey paths refer to the downwelling periods shown in Figure 2. Period I shows a huge impact on plume location and depth while period II shows a moderate impact.

Those patterns are visible on the plume thickness at station *ogi01* (Figure 9). The summer plume is present there during high discharge and southward wind conditions as the plume propagates southwestward or during low flow and frequent wind reversals as the plume grows close to the mouth. The decrease in plume thickness at this station is correlated with northward wind: as the wind blows southward (blue), the plume grows at *ogi01*, while it disappears if northward winds events (red) remain strong enough and/or last long enough. The simulated presence of the plume at mid-June corresponds to the underestimation of brackish water at *riso*.

Figure 12 highlights the correlation between the plume thickness (volume/area) and the plume location. It reflects the rapid reaction of the plume to wind changes. During upwelling-favorable wind events, the mean plume thickness is rather small (< 4 m), as the CR plume spreads over a large area due to Ekman transport and ambient stratification. On the contrary, northward winds push the plume toward the Washington coast. The CR plume is pressed against the coast, weakening the stratification and deepening the plume in shallow shelf area North of the CR mouth, as downward velocity advects surface water down the water column. While moving northward during event I, the plume centroid deepens (with a mean thickness > 4 m) and decelerates. For comparison, the distance traveled by the centroid between May 22 and May 24 (start of I) is similar to the distance between May 24 and June 2. As its mean velocity drops, tidal oscillations plays a significant role in its displacement. The aforementioned behavior is described in detail by Cole and Hetland (2016), where the characteristics of vertical mixing in such plumes are discussed.

The plume area shows a strong correlation with the wind direction (Figure 13). During event I, the plume area is smaller than average, as the plume is driven to the coast. In the days following period I, the area grows again, as the wind-constrained plume propagates along the coast. As soon as the wind turns, the area covered by the plume increases sharply, and the far-field plume covers a larger part of the coastal ocean. The drop during downwelling event II is also due to the Ekman transport toward the coast. The area covered at the end of the upwelling-favorable wind is still significant, a large part being along the Oregon coast. By contrast, the decrease at the end of June is a direct consequence of the drop of the river discharge. As the centroid path suggested, the plume area before the second event (II) is far larger (Figure 12). This partly explains why the plume remains on the Oregon shelf after the downwelling event.

As explained above, the plume area and thickness evolve in exact opposite ways. This feature is not surprising considering that wind changes do not significantly alter the plume volume. The plume volume instead correlates with a time lag of a few days to the water discharge (not shown) as the bulge retains a significant part of the outgoing water.

Burla et al. (2010) showed that river discharge is the predominant factor of the interannual plume variability in May. In their analysis of the sea surface salinity anomaly, Burla et al. (2010) underscore that year 2006 exhibits saltier conditions than the climatological signal on both the Washington and Oregon shelves, although the river discharge is not sensibly lower than average for that period. Coastal upwelling partly explains this feature, due to the quasi uninterrupted long period of southward wind from the end of April until the last third of May.
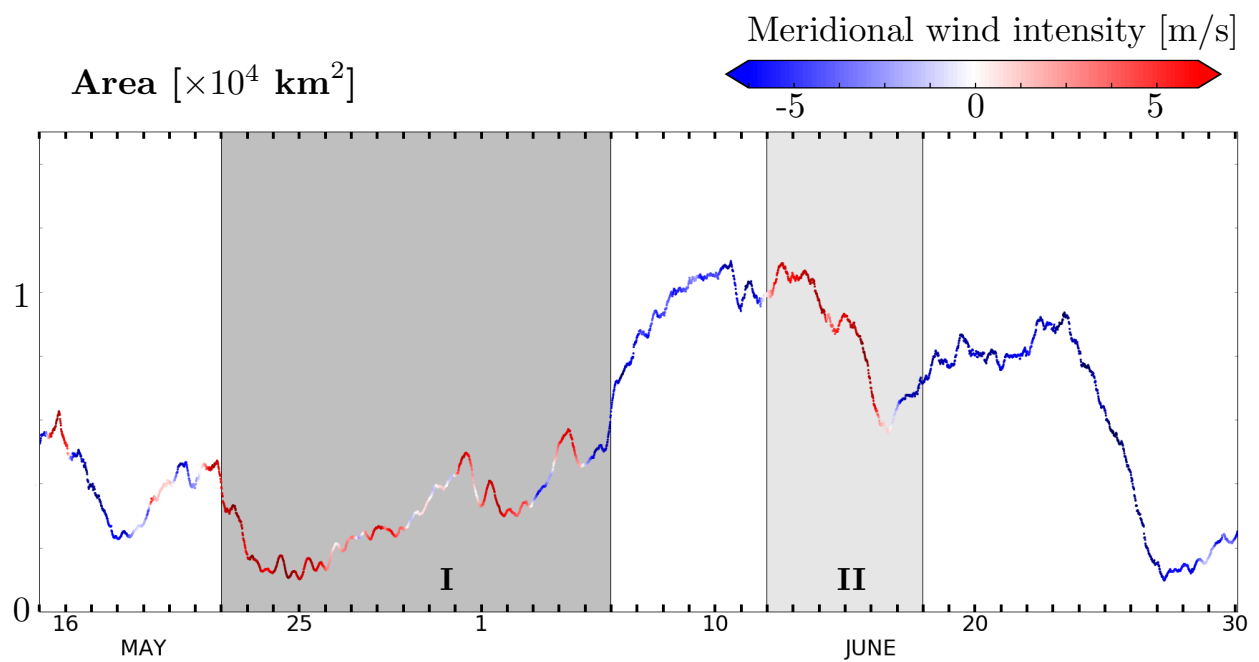
Figure 13: Timeserie of the surface area of the predicted plume, colored by meridional wind intensity. Downwelling-favorable wind events (red) tend to reduce the area, as the far-field plume becomes thinner along the Washington coast. On the contrary, upwelling-favorable winds (blue) transport the plume offshore where it can spread over a larger surface.

The prolongated freshet impacted the plume evolution of the following June.

Our study confirms the occurrence of bidirectional plumes (see Figure 10) in summer 2006 (Hickey and Banas, 2003; Horner-Devine et al., 2009; Liu et al., 2009a; Burla et al., 2010). As upwelling-favorable seasonal wind is often interrupted by wind reversals, Liu et al. (2009a) states that this behavior is representative of the majority of the 2004 summer season with a Self-Organizing Map (SOM) analysis. An empirical orthogonal function (EOF) analysis conducted over the period 1999-2006 by (Burla et al., 2010) confirms the leading mode of variability in summer is bimodal and accounts for 51% of the variance. Downwelling-favorable winds enhance the Coriolis effect to the North of the emerging plume. Medium to strong upwelling events annihilate this feature and drives the majority of the plume offshore in the south-west direction. The mean California Current further advects the plume to the South.

5   Discussion and conclusions

Coastal impact studies rely on accurate simulations of currents in the estuary and the coastal sea, and their complex interactions. The hydrodynamics is the foundation on which ecological or geochemical models are built. In this study, we describe the latest version of SLIM 3D, a hydrodynamical model aimed at bridging the gap between the estuary and the coastal sea. To suitably model such a complex continuum, SLIM 3D offers several advantages: (1) multi-scale phenomena are simulated seamlessly in a single mesh model; (2) the use of an unstructured mesh allows for a detailed representation of small-scale features of the topography; (3) the discontinuous Galerkin formulation provides high accuracy and robustness for this advection-dominated problem. Here, we simulate the hydrodynamics of the CR estuary and coastal sea during May-June 2006, a period characterized by high river discharge and strong changes in wind regime. Quantitative statistics evaluate the model skill and integrative metrics facilitate the analysis by highlighting the evolution of the CR plume in response to wind and river forcings.

The results show the ability of SLIM 3D to capture both the salinity intrusion in the estuary and the rapid response of the CR plume to wind reversals. SLIM 3D is able to reproduce the offshore advection of the northern coastal plume at the beginning of upwelling-favorable wind events. The discontinuous Galerkin numerical discretization allows SLIM 3D to handle gradients of bathymetry, velocity and density with minimal numerical dissipation. By introducing a new splitting between the 2D and 3D momentum equations, we markedly improved the representation of large-scale flow structures. We observe that it reduces the dissipation, as the coupling between internal and external modes is much more accurate.

Our model stands the comparison with other models of the CR estuary-plume dynamics. Inside the estuary, SLIM 3D compares well to an operational implementation of SELFE (same mean correlation coefficient). On the shelf, SLIM 3D correctly represents the large-scale flow structures despite using a rather coarse mesh resolution. It correctly reproduces the occurrence of a bidirectional plume as well as the wind-driven coastal upwelling. These features favorably compares to those obtained with ROMS. Despite a finer mesh resolution, SELFE yields overly

| Variable [unit] | Station | Skill metrics | | | | | | | |
| | | SLIM 3D | | | | SELFE | | | |
		Bias	RMSE	NMSE	Corr	Bias	RMSE	NMSE	Corr
Elevation [m]	tpoin	-0.06	0.19	0.05	0.98	-0.04	0.13	0.02	0.99
Elevation [m]	skaw1	-0.14	0.20	0.08	0.98	-0.06	0.12	0.03	0.99
Salinity [‰]	dsdma 7.3 m	-4.03	5.83	0.38	0.91	-1.35	4.84	0.27	0.89
Salinity [‰]	red26 7.5 m	-4.55	6.27	0.37	0.91	-1.32	4.87	0.23	0.90
Salinity [‰]	sandi 7.9 m	-1.32	5.37	0.27	0.88	-2.94	5.29	0.26	0.91
Salinity [‰]	tansy 8.4 m	-3.15	5.52	0.40	0.85	-0.56	4.36	0.27	0.86
Temperature [° C]	dsdma 7.3 m	-0.39	0.98	0.29	0.90	0.54	1.19	0.45	0.84
Temperature [° C]	red26 7.5 m	-0.46	1.13	0.29	0.87	0.30	1.12	0.31	0.85
Temperature [° C]	sandi 7.9 m	-0.60	1.32	0.48	0.82	1.11	1.54	0.71	0.82
Temperature [° C]	tansy 8.4 m	-0.14	1.13	0.31	0.84	0.83	1.31	0.44	0.86

Table 1: Skill metrics achieved by SLIM 3D for different variables and at different locations in the CR estuary. The NMSE is always below 0.5, which indicates that the model error is less than half of the observed variability. Correlations are very high for the elevation (0.98) and high for temperature and salinity (≥ 0.82). Stations locations are shown in Figure 3. SELFE model skill metrics are shown as a comparison.

smoothed fronts and seems to underestimate upwelling. Based on this study and on our previous experience with the model, we suggest that SLIM 3D skill is directly linked to the 2D-3D mode-splitting procedure and to the discontinuous Galerkin discretization. The former notably reduces the level of numerical dissipation, particularly for baroclinic processes. The latter provides a high-level of flexibility to resolve small-scale processes even on relatively coarse meshes. Such a combination of a consistent model formulation with a flexible numerical scheme seems ideally-suited to coastal applications.

Acknowledgment

A Skill metrics

Statistics obtained by comparing SLIM 3D model outputs with observations displayed in Figs 5, 7 and 8 are detailed in Tables 1 and 2.

Variable	Station	depth	Skill metrics							
			SLIM 3D				SELFE			
[unit]		[m]	Bias	RMSE	NMSE	Corr	Bias	RMSE	NMSE	Corr
Salinity [‰]	ogi01	0.8	-1.97	3.29	0.56	0.87	-1.03	3.52	0.62	0.72
Salinity [‰]	ogi01	5	0.53	2.16	0.82	0.51	-1.07	2.06	0.73	0.75
Salinity [‰]	ogi01	11	-0.02	0.68	0.91	0.43	-1.34	1.63	5.80	0.51
Salinity [‰]	ogi01	50	-0.39	0.55	1.69	0.46	-1.48	1.50	12.96	0.78
Salinity [‰]	rice	1	-2.90	5.51	1.21	0.53	-1.97	4.72	0.86	0.61
Salinity [‰]	rice	5	-0.22	1.85	0.66	0.60	-2.11	3.10	1.83	0.53
Salinity [‰]	rice	20	-0.10	0.47	0.44	0.77	-1.55	1.70	6.37	0.33
Salinity [‰]	rino	1	-0.46	2.28	0.83	0.70	-0.69	2.42	0.94	0.45
Salinity [‰]	rino	20	-0.07	0.49	0.75	0.53	-1.17	1.23	5.27	0.73
Salinity [‰]	riso	1	0.29	1.93	0.75	0.62	-1.43	2.08	0.86	0.74
Salinity [‰]	riso	20	0.37	0.59	0.95	0.65	-0.86	1.00	2.89	0.49
Salinity [‰]	saturn02	1	-2.48	4.71	1.32	0.48	-3.40	5.40	1.68	0.50
Salinity [‰]	saturn02	5	-0.30	1.39	0.45	0.76	-2.57	3.45	2.83	0.42
Salinity [‰]	saturn02	17	-0.10	0.54	0.30	0.84	-1.64	1.87	3.87	0.41
Temperature [° C]	ogi01	0.8	-1.30	1.42	1.84	0.84	1.04	1.37	1.71	0.59
Temperature [° C]	ogi01	5	-1.64	1.82	2.44	0.73	0.90	1.48	1.78	0.33
Temperature [° C]	ogi01	11	-1.69	2.07	2.48	0.42	0.26	1.37	1.35	0.12
Temperature [° C]	ogi01	50	0.08	0.53	1.04	0.22	0.99	1.07	4.57	0.76
Temperature [° C]	rice	1	-1.32	1.65	1.72	0.64	0.61	1.25	1.00	0.61
Temperature [° C]	rice	5	-1.68	1.99	2.01	0.66	0.65	1.42	1.07	0.55
Temperature [° C]	rice	20	-0.72	1.61	0.98	0.48	0.72	1.98	1.56	0.04
Temperature [° C]	rino	1	-1.27	1.43	0.74	0.92	0.75	1.14	0.47	0.86
Temperature [° C]	rino	20	-0.40	1.23	0.90	0.47	0.93	1.51	1.42	0.53
Temperature [° C]	riso	1	-0.91	1.44	0.70	0.78	0.77	1.71	1.08	0.42
Temperature [° C]	riso	20	-1.29	1.73	1.32	0.72	-0.59	1.41	0.93	0.49
Temperature [° C]	saturn02	1	-1.19	1.56	1.12	0.73	0.44	1.06	0.53	0.75
Temperature [° C]	saturn02	5	-1.50	1.95	1.30	0.69	0.84	1.64	1.01	0.54
Temperature [° C]	saturn02	17	-1.15	1.94	0.98	0.73	0.47	2.09	1.19	0.11

Table 2: Skill metrics achieved with SLIM 3D for different variables and at different locations on the Oregon and Washington shelves. SELFE model skill metrics are shown as a comparison.

References

Baptista, A. M., Seaton, C., Wilkin, M. P., Riseman, S. F., Needoba, J. A., Maier, D., Turner, P. J., Kärnä, T., Lopez, J. E., Herfort, L., Megler, V. M., McNeil, C., Crump, B. C., Peterson, T. D., Spitz, Y. H., and Simon, H. M. (2015). Infrastructure for collaborative science and societal applications in the Columbia River estuary. *Frontiers of Earth Science*, 9(4):659–682.

Baptista, A. M., Zhang, Y., Chawla, A., Zulauf, M., Seaton, C., Myers, E. P., Kindle, J., Wilkin, M., Burla, M., and Turner, P. J. (2005). A cross-scale model for 3d baroclinic circulation in estuary–plume–shelf systems: II. Application to the Columbia River. *Continental Shelf Research*, 25(7–8):935–972.

Blaise, S., Comblen, R., Legat, V., Remacle, J.-F., Deleersnijder, E., and Lambrechts, J. (2010). A discontinuous finite element baroclinic marine model on unstructured prismatic meshes. *Ocean Dynamics*, 60(6):1371–1393.

Burla, M., Baptista, A. M., Zhang, Y., and Frolov, S. (2010). Seasonal and interannual variability of the Columbia River plume: A perspective enabled by multiyear simulation databases. *Journal of Geophysical Research*, 115.

Canuto, V. M., Howard, A., Cheng, Y., and Dubovikov, M. S. (2001). Ocean Turbulence. Part I: One-Point Closure Model–Momentum and Heat Vertical Diffusivities. *Journal of Physical Oceanography*, 31(6):1413–1426.

Chassignet, E. P., Hurlburt, H. E., Smedstad, O. M., Halliwell, G. R., Hogan, P. J., Wallcraft, A. J., Baraille, R., and Bleck, R. (2007). The HYCOM (HYbrid Coordinate Ocean Model) data assimilative system. *Journal of Marine Systems*, 65(14):60–83.

Chawla, A., Jay, D. A., Baptista, A. M., Wilkin, M., and Seaton, C. (2008). Seasonal Variability and Estuary–Shelf Interactions in Circulation Dynamics of a River-dominated Estuary. *Estuaries and Coasts*, 31(2):269–288.

Cole, K. L. and Hetland, R. D. (2016). The Effects of Rotation and River Discharge on Net Mixing in Small-Mouth Kelvin Number Plumes. *Journal of Physical Oceanography*, 46(5):1421–1436.

Comblen, R., Blaise, S., Legat, V., Remacle, J.-F., Deleersnijder, E., and Lambrechts, J. (2010). A discontinuous finite element baroclinic marine model on unstructured prismatic meshes. *Ocean Dynamics*, 60(6):1395–1414.

Davis, K. A., Banas, N. S., Giddings, S. N., Siedlecki, S. A., MacCready, P., Lessard, E. J., Kudela, R. M., and Hickey, B. M. (2014). Estuary-enhanced upwelling of marine nutrients fuels coastal productivity in the U.S. Pacific Northwest. *Journal of Geophysical Research: Oceans*, 119(12):8778–8799.

de Boer, G. J., Pietrzak, J. D., and Winterwerp, J. C. (2008). Using the potential energy anomaly equation to investigate tidal straining and advection of stratification in a region of freshwater influence. *Ocean Modelling*, 22(1-2):1–11.

de Brye, B., de Brauwere, A., Gourgue, O., Kärnä, T., Lambrechts, J., Comblen, R., and Deleersnijder, E. (2010). A finite-element, multi-scale model of the Scheldt tributaries, river, estuary and ROFI. *Coastal Engineering*, 57(9):850–863.

de Brye, B., Schellen, S., Sassi, M., Vermeulen, B., Kärnä, T., Deleersnijder, E., and Hoitink, T. (2011). Preliminary results of a finite-element, multi-scale model of the Mahakam Delta (Indonesia). *Ocean Dynamics*, 61(8):1107–1120.

Delandmeter, P., Lewis, S. E., Lambrechts, J., Deleersnijder, E., Legat, V., and Wolanski, E. (2015). The transport and fate of riverine fine sediment exported to a semi-open system. *Estuarine, Coastal and Shelf Science*, 167:336–346.

Egbert, G. D. and Erofeeva, S. Y. (2002). Efficient inverse modeling of barotropic ocean tides. *Journal of Atmospheric and Oceanic Technology*, 19(2):183–204.

Fiedler, P. C. and Laurs, R. M. (1990). Variability of the Columbia River plume observed in visible and infrared satellite imagery. *International Journal of Remote Sensing*, 11(6):999–1010.

Garcia Berdeal, I., Hickey, B. M., and Kawase, M. (2002). Influence of wind stress and ambient flow on a high discharge river plume. *Journal of Geophysical Research: Oceans*, 107(C9):3130.

Geuzaine, C. and Remacle, J.-F. (2009). Gmsh: A 3-D finite element mesh generator with built-in pre- and post-processing facilities. *International Journal for Numerical Methods in Engineering*, 79(11):1309–1331.

Geyer, W. R. and MacCready, P. (2014). The Estuarine Circulation. *Annual Review of Fluid Mechanics*, 46(1):175–197.

Giddings, S. N., MacCready, P., Hickey, B. M., Banas, N. S., Davis, K. A., Siedlecki, S. A., Trainer, V. L., Kudela, R. M., Pelland, N. A., and Connolly, T. P. (2014). Hindcasts of potential harmful algal bloom transport pathways on the Pacific Northwest coast. *Journal of Geophysical Research: Oceans*, 119(4):2439–2461.

Haidvogel, D. B., Arango, H. G., Hedstrom, K., Beckmann, A., Malanotte-Rizzoli, P., and Shchepetkin, A. F. (2000). Model evaluation experiments in the North Atlantic Basin: simulations in nonlinear terrain-following coordinates. *Dynamics of Atmospheres and Oceans*, 32(3–4):239–281.

Haney, R. L. (1991). On the Pressure Gradient Force over Steep Topography in Sigma Coordinate Ocean Models. *Journal of Physical Oceanography*, 21(4):610–619.

Hickey, B., Geier, S., Kachel, N., and MacFadyen, A. (2005). A bi-directional river plume: The Columbia in summer. *Continental Shelf Research*, 25(14):1631–1656.

Hickey, B., McCabe, R., Geier, S., Dever, E., and Kachel, N. (2009). Three interacting freshwater plumes in the northern California Current System. *Journal of Geophysical Research: Oceans*, 114(C2):C00B03.

Hickey, B. M. and Banas, N. S. (2003). Oceanography of the US Pacific Northwest coastal ocean and estuaries with application to coastal ecology. *Estuaries and Coasts*, 26(4):1010–1031.

Hickey, B. M., Kudela, R. M., Nash, J. D., Bruland, K. W., Peterson, W. T., MacCready, P., Lessard, E. J., Jay, D. A., Banas, N. S., Baptista, A. M., Dever, E. P., Kosro, P. M., Kilcher, L. K., Horner-Devine, A. R., Zaron, E. D., McCabe, R. M., Peterson, J. O., Orton, P. M., Pan, J., and Lohan, M. C. (2010). River Influences on Shelf Ecosystems: Introduction and synthesis. *Journal of Geophysical Research: Oceans*, 115(C2):C00B17.

Hickey, B. M., Pietrafesa, L. J., Jay, D. A., and Boicourt, W. C. (1998). The Columbia River Plume Study: Subtidal variability in the velocity and salinity fields. *Journal of Geophysical Research: Oceans*, 103(C5):10339–10368.

Higdon, R. L. and de Szoeke, R. A. (1997). Barotropic-Baroclinic Time Splitting for Ocean Circulation Modeling. *Journal of Computational Physics*, 135(1):30–53.

Horner-Devine, A. R., Jay, D. A., Orton, P. M., and Spahn, E. Y. (2009). A conceptual model of the strongly tidal Columbia River plume. *Journal of Marine Systems*, 78(3):460–475.

Jackett, D. R., McDougall, T. J., Feistel, R., Wright, D. G., and Griffies, S. M. (2006). Algorithms for Density, Potential Temperature, Conservative Temperature, and the Freezing Temperature of Seawater. *Journal of Atmospheric and Oceanic Technology*, 23(12):1709–1728.

Kärnä, T. and Baptista, A. M. (2016a). Evaluation of a long-term hindcast simulation for the Columbia River estuary. *Ocean Modelling*, 99:1–14.

Kärnä, T. and Baptista, A. M. (2016b). Water age in the Columbia River estuary. *Estuarine, Coastal and Shelf Science*, 183, Part A:249–259.

Kärnä, T., Baptista, A. M., Lopez, J. E., Turner, P. J., McNeil, C., and Sanford, T. B. (2015). Numerical modeling of circulation in high-energy estuaries: A Columbia River estuary benchmark. *Ocean Modelling*, 88:54–71.

Kärnä, T., Legat, V., and Deleersnijder, E. (2013). A baroclinic discontinuous Galerkin finite element model for coastal flows. *Ocean Modelling*, 61:1–20.

Kärnä, T., Legat, V., Deleersnijder, E., and Burchard, H. (2012). Coupling of a discontinuous Galerkin finite element marine model with a finite difference turbulence closure model. *Ocean Modelling*, 47:55–64.

Lambrechts, J., Hanert, E., Deleersnijder, E., Bernard, P.-E., Legat, V., Remacle, J.-F., and Wolanski, E. (2008). A multi-scale model of the hydrodynamics of the whole Great Barrier Reef. *Estuarine, Coastal and Shelf Science*, 79(1):143–151.

Le Bars, Y., Vallaeys, V., Deleersnijder, E., Hanert, E., Carrere, L., and Channelière, C. (2016). Unstructured-mesh modeling of the Congo river-to-sea continuum. *Ocean Dynamics*, 66(4):589–603.

Liu, Y., MacCready, P., and Hickey, B. M. (2009a). Columbia River plume patterns in summer 2004 as revealed by a hindcast coastal ocean circulation model. *Geophysical Research Letters*, 36(2). L02601.

Liu, Y., MacCready, P., Hickey, B. M., Dever, E. P., Kosro, P. M., and Banas, N. S. (2009b). Evaluation of a coastal ocean circulation model for the Columbia River plume in summer 2004. *Journal of Geophysical Research*, 114.

Lopez, J. E. and Baptista, A. M. (2017). Benchmarking an unstructured grid sediment model in an energetic estuary. *Ocean Modelling*, 110:32–48.

MacCready, P., Banas, N. S., Hickey, B. M., Dever, E. P., and Liu, Y. (2009). A model study of tide- and wind-induced mixing in the Columbia River Estuary and plume. *Continental Shelf Research*, 29(1):278–291.

Murphy, A. H. (1988). Skill Scores Based on the Mean Square Error and Their Relationships to the Correlation Coefficient. *Monthly Weather Review*, 116(12):2417–2424.

Pham Van, C., de Brye, B., Deleersnijder, E., Hoitink, A. J. F., Sassi, M., Spinewine, B., Hidayat, H., and Soares-Frazão, S. (2016). Simulations of the flow in the Mahakam river–lake–delta system, Indonesia. *Environmental Fluid Mechanics*, 16(3):603–633.

Phillips, E. M., Horne, J. K., and Zamon, J. E. (2017). Predator-prey interactions influenced by a dynamic river plume. *Canadian Journal of Fisheries and Aquatic Sciences*.

Ringler, T., Petersen, M., Higdon, R. L., Jacobsen, D., Jones, P. W., and Maltrud, M. (2013). A multi-resolution approach to global ocean modeling. *Ocean Modelling*, 69:211–232.

Smagorinsky, J. (1963). General circulation experiments with the primitive equations: I. the basic experiment. *Monthly weather review*, 91(3):99–164.

Smith, S. D. and Banke, E. G. (1975). Variation of the sea surface drag coefficient with wind speed. *Quarterly Journal of the Royal Meteorological Society*, 101(429):665–673.

Taylor, K. E. (2001). Summarizing multiple aspects of model performance in a single diagram. *Journal of Geophysical Research: Atmospheres*, 106(D7):7183–7192.

Thomas, C. J., Lambrechts, J., Wolanski, E., Traag, V. A., Blondel, V. D., Deleersnijder, E., and Hanert, E. (2014). Numerical modelling and graph theory tools to study ecological connectivity in the Great Barrier Reef. *Ecological Modelling*, 272:160–174.

Vincent, D., Karatekin, Ö., Vallaeys, V., Hayes, A. G., Mastrogiuseppe, M., Notarnicola, C., Dehant, V., and Deleersnijder, E. (2016). Numerical study of tides in Ontario Lacus, a hydrocarbon lake on the surface of the Saturnian moon Titan. *Ocean Dynamics*, 66(4):461–482.

White, L., Deleersnijder, E., and Legat, V. (2008). A three-dimensional unstructured mesh finite element shallow-water model, with application to the flows around an island and in a wind-driven, elongated basin. *Ocean Modelling*, 22(1–2):26–47.

Zhang, Y. and Baptista, A. M. (2004). Benchmarking a new open-source 3d circulation model (ELCIRC). In Pinder, C. T. M. a. G. F., editor, *Developments in Water Science*, volume 55, Part 2 of *Computational Methods in Water Resources: Volume 2Proceedings of the XVth International Conference on Computational Methods in Water Resources*, pages 1791–1800. Elsevier. DOI: 10.1016/S0167-5648(04)80185-0.

Zhang, Y. and Baptista, A. M. (2008). SELFE: A semi-implicit Eulerian–Lagrangian finite-element model for cross-scale ocean circulation. *Ocean Modelling*, 21(3–4):71–96.

Zhang, Y., Baptista, A. M., and Myers, E. P. (2004). A cross-scale model for 3d baroclinic circulation in estuary–plume–shelf systems: I. Formulation and skill assessment. *Continental Shelf Research*, 24(18):2187–2214.